Brain state and cortical layer-specific mechanisms underlying perception at threshold

Mitchell P. Morton[1,2], Sachira Denagamage[1,2], Isabel J. Blume[1], John H. Reynolds[4], Monika P. Jadi[1,2,3] and Anirvan S. Nandy[1,2]
[1]Department of Neuroscience, Yale University, New Haven, CT 06511
[2]Interdepartmental Neuroscience Program, Yale University, New Haven, CT 06511
[3]Department of Psychiatry, Yale University, New Haven, CT 06511
[4]Systems Neurobiology Laboratories, The Salk Institute for Biological Studies, La Jolla, CA 92037
Correspondence: anirvan.nandy@yale.edu

ABSTRACT

Identical stimuli can be perceived or go unnoticed across successive presentations, producing divergent behavioral readouts despite similarities in sensory input. We hypothesized that fluctuations in neurophysiological states in the sensory neocortex, which could alter cortical processing at the level of neural subpopulations, underlies this perceptual variability. We analyzed cortical layer-specific electrophysiological activity in visual area V4 during a cued attention task. We find that hit trials are characterized by a larger pupil diameter and lower incidence of microsaccades, indicative of a behavioral state with increased arousal and perceptual stability. Target stimuli presented at perceptual threshold evoke elevated multi-unit activity in V4 neurons in hit trials compared to miss trials, across all cortical layers. Putative excitatory and inhibitory neurons are strongly positively modulated in the input (IV) and deep (V & VI) layers of the cortex during hit trials. Excitatory neurons in the superficial cortical layers exhibit lower variability in hit trials. Deep layer neurons are less phase-locked to low frequency rhythms in hits. Hits are also characterized by greater interlaminar coherence between the superficial and deep layers in the pre-stimulus period, and a complementary pattern between the input layer and both the superficial and deep layers in the stimulus-evoked period. Taken together, these results indicate that a state of elevated levels of arousal and perceptual

29 stability allow enhanced processing of sensory stimuli, which contributes to hits at
30 perceptual threshold.

INTRODUCTION

Physical properties of stimuli strongly influence perception. Low intensity stimuli are detected infrequently. As intensity increases, detection probability remains low until some perceptual threshold is crossed, after which stimuli are perceived robustly. A psychometric function (Prins and Kingdom, 2018; Watson, 1979; Wichmann and Hill, 2001) mathematically describes this property of perception. Only within a narrow range around the perceptual threshold do stimuli lead to significant trial-to-trial perceptual variance. While many studies present stimuli at threshold (Herman et al., 2017; Levitt, 1971; Pins and ffytche, 2003; Ress and Heeger, 2003), few have probed the cortical microcircuit mechanisms that underlie successful or unsuccessful perception under these conditions (McCormick et al., 2020; van Vugt et al., 2018).

Prior studies have characterized how perceived stimuli trigger stronger information propagation from earlier visual areas to higher order visual and frontal regions (Herman et al., 2017; van Vugt et al., 2018). Information propagation and sensory processing are strongly influenced by brain states such as arousal and attention (Harris and Thiele, 2011; McCormick et al., 2020). Arousal has long been known to modulate cortical activity (Livingstone and Hubel, 1981; McCormick and Bal, 1997) and impact behavioral performance on a variety of sensory tasks (Aston-Jones and Cohen, 2005; McGinley et al., 2015; Yerkes and Dodson, 1908). Activity in visual area V4, a critical intermediate region in the ventral visual processing stream (Goodale and Milner, 1992; Mountcastle, 1997; Roe et al., 2012) is known to be strongly modulated by attention (Desimone and Duncan, 1995; McAdams and Maunsell, 1999; Moran and Desimone, 1985; Reynolds et al., 2000). Attention enhances the firing rates of V4 neurons, increases the reliability in firing of individual neurons, and decreases correlated fluctuations among pairs of neurons

(Cohen and Maunsell, 2009; McAdams and Maunsell, 1999; Mitchell et al., 2007, 2009).

The visual cortex has a columnar architecture, in which multiple cell classes (Connors and Gutnick, 1990; Markram et al., 2004; Migliore and Shepherd, 2005; Wonders and Anderson, 2006; Zeng and Sanes, 2017) across the cortical layers (Douglas and Martin, 2004; Mountcastle, 1997) form distinct sub-populations. These sub-populations form a canonical microcircuit that orchestrates the encoding and flow of information (Douglas and Martin, 2007; Hirsch and Martinez, 2006). These sub-populations contribute uniquely to sensory processing and are differentially modulated by brain states (McCormick et al., 1985; Mitchell et al., 2007; Nandy et al., 2017; Pettine et al., 2019). However, the role of these subpopulations in sensory processing at perceptual threshold remain poorly understood. Moreover, the influence of brain states, that may be responsible for different outcomes at threshold, on these sub-populations has not been studied in detail.

Here we examine the neural mechanisms that regulate perception at threshold. We specifically focus on the columnar microcircuit mechanisms within area V4. We hypothesized that minor fluctuations in behavioral state, such as arousal and perceptual stability, influence the activity of neural sub-populations within the visual cortex, and thereby result in different perceptual outcomes at threshold.

RESULTS

To study the neural dynamics responsible for determining whether a stimulus presented at perceptual threshold is perceived, we analyzed behavioral and cortical layer-specific neural data from area V4, collected while monkeys performed a cued attention task

(Nandy et al., 2017). Monkeys were trained to detect an orientation change in one of two Gabor stimuli that were presented concurrently at two spatial locations, and to report having seen the change by making an eye movement to the changed stimulus. Prior to a block of trials, monkeys were cued as to which of the two spatial locations was likely to undergo the orientation change (95% valid cue). During a trial, “non-target” stimuli at a fixed reference orientation were repeatedly presented. Non-targets were turned on for 200ms at the two spatial locations, and then turned off for a variable interval (200-400ms). At a random time (1-5s, mean 3s) a “target” stimulus, differing in orientation from the non-targets, was presented at one of the locations. If the monkey reported having detected the orientation change by making an eye movement to the location of the changed stimulus, it received a juice reward (Figure 1A, “hit” trial). If the monkey failed to detect the orientation change and instead continued to maintain fixation on the center of the monitor it was not rewarded (Figure 1A, “miss” trial). In this study, we focused exclusively on trials in which the target stimulus was presented at the cued location (95% of trials).

On each trial, the magnitude of the orientation change was drawn from a distribution that spanned multiple levels of difficulty. We fit the behavioral data with a logistic function (Prins and Kingdom, 2018) and defined the threshold condition as the orientation change that was closest to the 50% threshold of the fitted psychometric function for that session (Figure 1B, Experimental Procedures). We selected this subset of trials for further analysis, since the constant target stimuli in these trials were equally likely to be perceived or not perceived.

While monkeys performed this task, single- and multi-unit activity and local field potentials (LFPs) were recorded in area V4 using 16-channel linear array electrodes

(Plexon inc., Figure S1A-E). The array was inserted perpendicular to the cortical surface and spanned the cortical layers. We used current source density (CSD) analysis (Mitzdorf, 1985) to estimate the boundaries between the superficial (I-III), input (IV), and deep (V-VI) cortical layers (Figure S1E-F), and assign individual neurons their layer identity (Mitchell et al., 2007; Nandy et al., 2017). Single units were classified as either broad-spiking (putative excitatory neurons) or narrow-spiking (putative inhibitory neurons) on the basis of their waveform width (peak to trough duration; Figure S1D; see Experimental Procedures; Connors and Gutnick, 1990; Kawaguchi, 1993; McCormick et al., 1985; Nandy et al., 2017; Nowak et al., 2003). Eye position and pupil diameter were also recorded (ISCAN ETL-200).

To assess the behavioral impact of variations in arousal and perceptual stability across trials and the threshold condition, we compared pupil diameter and microsaccade incidence across trail outcomes. Larger pupil diameter is thought to be a proxy for elevated alertness and arousal (Aston-Jones and Cohen, 2005; Beatty and Lucero-Wagoner, 2000; Hess and Polt, 1964; McCormick et al., 2020; McGinley et al., 2015; Reimer et al., 2014; Tang and Higley, 2020). We found that hit trials were associated with larger pupil diameters compared to miss trials, both before and during stimulus presentations (Figure 2A). We quantified this difference in the estimation statistics framework (Calin-Jageman and Cumming, 2019; Ho et al., 2019) by comparing effect sizes and using bootstrapping to estimate uncertainty in the differences. We found that the mean of the distribution of pupil diameters associated with hit trials is greater than that associated with misses (Figure 2B; complementary null hypothesis testing results in Table 1). In both hit and miss trials, the mean pupil diameter was close to the optimal

arousal state for perceptual performance (Figure 2C; McGinley et al., 2015). Our results suggest that hits are more likely to occur during periods of greater arousal.

Microsaccades, small fixational eye movements of <1° in amplitude that occur during normal fixation, are associated with periods of decreased perceptual stability (Dicke et al., 2008; Zuber and Stark, 1966). Microsaccades have been linked to suppressed neural responses in visual areas during perceptual tasks, impairing fine visual discrimination and behavioral performance (Beeler, 1967; Hafed and Krauzlis, 2010). We grouped trials in the threshold condition based on whether a microsaccade occurred in a 400ms window preceding the onset of the target stimulus. Most trials with a pre-target microsaccade were misses, whereas the majority of trials without a microsaccade in this window were hits (Figure 2D; X^2 proportion test, $p < 0.001$). Consistent with previous reports (Lowet et al., 2018) we also find that microsaccades toward the attended stimulus were overrepresented in correct trials (Figure S2A, upper left). Conversely, microsaccades towards the attended stimulus were underrepresented in incorrect trials (Figure S2A, lower left). There was a very low but statistically significant negative correlation between pupil diameter and microsaccade rate (Figure S2B, $r^2 = 0.006$, $p < 0.001$). Overall, these results suggest that successful trials at threshold are significantly more likely to occur during a state of greater arousal and perceptual stability.

Having established that hit trials are more likely to occur in states of elevated arousal and perceptual stability, we investigated whether hits are characterized by differential information processing in V4. Elevated stimulus-evoked firing rates in hits would indicate a stronger representation of the stimulus that could be necessary for accurate discrimination. We compared the firing rates of all neurons (single and multi-

147 units) recorded in each cortical layer across hit and miss trials. For non-target stimuli,
148 firing rates were equivalent for hits and misses in both the pre-stimulus (0-200ms before
149 stimulus onset) and stimulus-evoked (60-260ms following stimulus onset) periods (Figure
150 3A). For the target stimulus, firing rates were once again equivalent in the pre-stimulus
151 period, but hit trials were characterized by elevated firing across cortical layers in the
152 stimulus-evoked period (Figure 3B-C). Broad and narrow-spiking neurons in both the
153 input and deep layers respond more to target stimuli in hit trials, and trend towards
154 elevated firing rates in the superficial layers during hits (Figure 3D). The average firing
155 rate in response to target stimuli for each neuron is shown in Figure S3 for both hit and
156 miss trials.

157 Variability in response reflects how reliably information is encoded by a neural
158 population. Lower baseline variability can enhance the ability of neurons to encode
159 stimulus differences. We calculated the Fano factor, a mean-normalized measure of trial-
160 to-trial variability in firing, for single-units in our population (Figure 4A). We find that broad-
161 spiking units in the superficial layer exhibited lower Fano factor during the pre-stimulus
162 period in hit trials (0-60ms before stimulus onset, Figure 4B), indicating this population of
163 neurons fired more reliably when the animal correctly detected the orientation change.
164 This was not the case for broad-spiking neurons in other layers (Figure 4B) or narrow-
165 spiking neurons (data not shown).

166 We next wanted to test how the relationship between spiking activity and LFPs
167 may differ across hits and misses. Spike-LFP synchrony can reflect cortical processing
168 and both within- and inter-areal coordination (Fries, 2009; Fries et al., 2008; Siapas et al.,
169 2005). We calculated the PPC (Vinck et al., 2010), a frequency resolved measure of

spike-LFP phase-locking, for single and multi-units relative to their local LFP signal during the pre-stimulus period (0-200ms before stimulus onset, Figure 5A). We averaged PPC values at low (3-12Hz), medium (15-25Hz), and high (30-80Hz) frequency bands (superficial & Input: Figure S4A-B; deep: Figure 5B & S4C). Deep layer neurons exhibit reduced low-frequency phase-locking in hit trials than in misses (Figure 5B), suggesting an improvement in pooled signal-to-noise among this neural population.

Our results at the individual neuron or neural-subpopulation levels suggest enhanced processing of perceived stimuli. However, it is the concerted activity among neural sub-populations that ultimately determine information flow through the laminar cortical circuit. We therefore examined differences in interlaminar synchrony as signatures of differential information flow between hit and miss trials. Spike-spike coherence (SSC) is a frequency resolved measure of the degree to which two spike trains fluctuate together (Mitchell et al., 2009; Mitra and Pesaran, 1999). We measured interlaminar SSC for spike trains from pairs of cortical layers, each spike train being comprised of all recorded action potentials in a given layer (See Experimental Procedures). We computed interlaminar SSC separately for hit and mis trials in both the pre-stimulus (0-200ms before stimulus onset, Figure 6A) and stimulus-evoked (60-260ms after stimulus onset, Figure 7A) periods. We averaged SSC for each pair of layers across three frequency bands, 3-12Hz, 15-25Hz, and 30-80Hz (Figure 6B and 7B).

Overall, hit trials have greater interlaminar SSC in hits compared to misses at almost all frequencies (Figure 6B and 7B). In the pre-stimulus period, the strongest SSC difference between hits and misses was observed between the superficial and deep layers across all frequencies (Figure 6B, middle panel). This implies greater synchrony of

the output layers of the cortex during hit trials. In contrast, this pattern was the opposite in the stimulus-evoked period, with greater SSC differences being found in pairs that involve the input layer (Figure 7B, top and bottom). This may reflect a higher degree of stimulus-driven feed-forward information propagation during hit trials. When comparing across time (pre-stimulus vs stimulus-evoked), layers, and frequency band, there was a significant interaction effect of layer pair and time window (three-way ANOVA, $p = 0.0075$).

Finally, we sought to compare the predictive power of our results on the monkey's perceptual performance. We created a generalized linear model (GLM) to regress behavioral outcome from the pupil diameter, number of microsaccades in the pre-target window, and average target-evoked multi-unit firing rate in each of the three layers (see Experimental Procedures; Davis et al., 2020). Other reported measures (Fano factor, PPC, interlaminar SSC) that we could not estimate reliably on a single trial basis were not considered in the GLM analysis. Pre-target microsaccades were by far the strongest predictor of performance ($weight = -1.3116$; $p = 6.0757e-08$). Input layer firing rate also significantly predicted perception ($weight = 0.3276$; $p = 0.020068$). Superficial firing rate, deep firing rate, and pupil diameter were not significant predictors (Table 2, all $p > 0.5$). This indicates that perceptual stability in the pre-target window is critical for behavioral performance, and elevated firing in the input layer is the most reliable physiological signature of a perceived stimulus.

DISCUSSION

We investigated the physiological processes responsible for variable behavioral outcomes at perceptual threshold. Controlling for *both* the attentive instruction (thus

minimizing large-scale attentional effects) and the stimulus condition that elicited performance at a threshold level allowed us to examine the physiological and neural correlates that underlie correct versus incorrect behavioral outcomes. We found multiple lines of evidence which suggest that a state of higher arousal and perceptual stability and the accompanying enhanced processing of visual stimuli contributes to accurate perception in hit trials.

Pupil diameter is elevated in hit trials (Figure 2A-C), and prior studies have shown that pupil diameter is strongly linked to arousal and alertness (Beatty and Lucero-Wagoner, 2000; Hess and Polt, 1964; Tang and Higley, 2020). This provides evidence that a state of higher arousal may contribute to improved sensory processing. The much lower hit rate in trials with a microsaccade preceding the target (Figure 2D) and our GLM analysis shows that perceptual stability is critical for accurate discrimination at threshold. It is unlikely that these two measures are reflecting the same phenomenon, as there is a very weak correlation between them over the course of a trial (Figure S2B).

There is a strong link between oculomotor control and attentional deployment (Moore and Fallah, 2001; Moore and Zirnsak, 2017; Schafer and Moore, 2011), and recent evidence suggests that microsaccades directed towards a target stimulus reflect attention-related processing and performance (Lowet et al., 2018). In our dataset, during the pre-target period, microsaccades towards the attended stimulus were overrepresented in correct trials (Figure S2A, upper left). Conversely, microsaccades towards the attended stimulus were underrepresented in incorrect trials (Figure S2A, lower left). Microsaccades directed towards the location of the eventual target may reflect elevated attentional deployment that can compensate for the perceptual instability due to

239 higher incidence of microsaccades.

240 Our electrophysiological findings associated with hit trials for threshold stimuli,
241 *within* a cued attention state, mirror several previous findings that are associated with the
242 deployment of covert spatial attention. Attention has long been known to increase firing
243 rates in V4 (McAdams and Maunsell, 1999; Mitchell et al., 2007; Spitzer et al., 1988), and
244 there is recent evidence that this increase occurs in all cortical layers in V4 (Nandy et al.,
245 2017). We find that elevated firing rates in hits occur across all layers in conjunction with
246 elevated arousal (Figure 3). Attention reduces the variability in the firing of V4 neurons,
247 and this reduction is thought to contribute to the improved information coding capacity of
248 a population of neurons (Cohen and Maunsell, 2009; Mitchell et al., 2007, 2009; Moreno-
249 Bote et al., 2014; Nandy et al., 2017). The reduction in Fano factor among broad-spiking
250 superficial-layer neurons in hit trials mirrors the effects of attention. Since these neurons
251 are putative projection neurons to downstream cortical areas, this reduction in Fano factor
252 may indicate increased reliability in stimulus encoding that could contribute to hits. Our
253 finding is also in agreement with previous reports of higher variability in representations
254 of unperceived stimuli in humans (Schurger et al., 2010). Synchronous neural activity
255 appears to modulate perceptual and cognitive ability in a variety of contexts (Abbas et al.,
256 2018; Fries et al., 2001; Rohenkohl et al., 2018; Worden et al., 2000). We found that
257 deep-layer neurons exhibit less low-frequency phase-locking in hit trials (Figure 5). This
258 is consistent with prior studies that find an attention-mediated reduction in the power
259 spectrum of the spike-triggered-averaged LFP (Fries et al., 2001).

260 Our examination of inter-laminar synchrony revealed two interesting and
261 complementary patterns: hits were associated with greater coherence between the

superficial and deep layers during spontaneous activity in the pre-stimulus period (Figure 6); in contrast, we found enhanced coherence between the input layer and both the output layers (superficial and deep) in the stimulus-evoked period during hits (Figure 7). Increased superficial-deep coherence in the pre-stimulus period could be the result of neuromodulatory or top-down processes that maintain the cortex in a state of sustained depolarization corresponding to a state of higher arousal during hits (McCormick et al., 2020; McGinley et al., 2015). Increased synchrony between the input layer and the output layers during the stimulus-evoked period could then reflect stronger information propagation through the cortical circuit, and hence with improved stimulus detection (Marshel et al., 2019). In contrast to broad global synchrony or local correlated fluctuations, which may signal a default state of minimal processing or decreased information coding capacity (Mitchell et al., 2009; Steriade et al., 1993; von Krosigk et al., 1993; Zohary et al., 1994), these patterns of interlaminar coherence that we found suggest that successful perception at threshold is mediated by pathway specific modulation of information flow through the laminar cortical circuit.

Several studies have examined how information flow differs for perceived and unperceived stimuli at a more macroscopic scale (Herman et al., 2017; van Vugt et al., 2018). van Vugt et al. (2018) recorded from three brain regions, V1, V4, and dorsolateral prefrontal cortex (dlPFC), while a monkey performed a stimulus detection task at threshold. Their work supports the model that feedforward propagation of sensory information from the visual cortex to the PFC causes a non-linear “ignition” of association areas resulting in conscious perception (Dehaene and Changeux, 2011). Herman et al. (Herman et al., 2017). found that conscious human perception triggers a wave of activity

propagation from occipital to frontal cortex while switching off default mode and other networks. Our study provides insight into the functions of the cortical microcircuit at the columnar level that could reflect these large-scale sweeping activity changes in perception.

Overall, we identified substantial layer-specific differences in cortical activity between hits and misses at perceptual threshold, during both the pre-stimulus and stimulus-evoked periods (Figure 8). These differences are indicative of greater fidelity of stimulus processing in hits, likely as a result of elevated arousal and perceptual stability. Synchrony analysis reveals a potential higher state of anticipatory engagement in the pre-stimulus period followed by improved signal propagation after stimulus presentation. These physiological differences in the laminar microcircuit likely contribute to successful perceptual discrimination at threshold.

EXPERIMENTAL PROCEDURES

Surgical Procedures

Surgical procedures have been described in detail previously (Nandy et al., 2017; Nassi et al., 2015; Ruiz et al., 2013). In brief, an MRI compatible low-profile titanium chamber was placed over the pre-lunate gyrus, on the basis of preoperative MRI in two rhesus macaques (right hemisphere in Monkey A, left hemisphere in Monkey C). The native dura mater was then removed, and a silicone based optically clear artificial dura (AD) was inserted, resulting in an optical window over dorsal V4 (Figure S1A, B). All procedures were approved by the Institutional Animal Care and Use Committee and conformed to NIH guidelines.

Electrophysiology

At the beginning of each recording session a plastic insert, with an opening for targeting electrodes, was lowered into the chamber and secured. This served to stabilize the recording site against cardiac pulsations. Neurons were recorded from cortical columns in dorsal V4 using 16-channel linear array electrodes ('laminar probes', Plexon Inc., Plexon V-probe). The laminar probes were mounted on adjustable X-Y stages attached to the recording chamber and positioned over the center of the pre-lunate gyrus under visual guidance through a microscope (Zeiss Inc., Figure S1C). This ensured that the probes were maximally perpendicular to the surface of the cortex and thus had the best possible trajectory to make a perpendicular penetration down a cortical column. Across recording sessions, the probes were positioned over different sites along the center of the gyrus in the parafoveal region of V4 with receptive field (RF) eccentricities between 2 and 7 degrees of visual angle. Care was taken to target cortical sites with no surface micro-vasculature, with surface micro-vasculature used as reference so that the same cortical site was not targeted across recording sessions. The probes were advanced using a hydraulic microdrive (Narishige Inc.) to first penetrate the AD and then through the cortex under microscopic visual guidance. Probes were advanced until the point that the top-most electrode (toward the pial surface) registered local field potential (LFP) signals. At this point, the probe was retracted by about 100-200 μm to ease the dimpling of the cortex due to the penetration. This procedure greatly increased the stability of the recordings and increased the neuronal yield in the superficial electrodes.

The distance from the tip of the probes to the first electrode contact was either 300 μm or 700 μm. The inter-electrode distance was 150 μm, thus minimizing the possibility

of recording the same neural spikes in adjacent recording channels. Electrical signals were recorded extracellularly from each channel. These were then amplified, digitized and filtered either between 0.5 Hz and 2.2 kHz (LFPs) or between 250 Hz and 8 kHz (spikes) and stored using the Multichannel Acquisition Processor system (MAP system, Plexon Inc.). Spikes and LFPs were sampled at 40 and 10 kHz respectively. LFP signals were further low-pass filtered with a 6^{th} order Butterworth filter with 300Hz cut-off and down-sampled to 1 kHz for further analysis. Spikes were classified as either multi-unit clusters or isolated single units using the Plexon Offline Sorter software program. Single units were identified based on two criteria: (a) if they formed an identifiable cluster, separate from noise and other units, when projected into the principal components of waveforms recorded on that electrode and (b) if the inter-spike interval (ISI) distribution had a well-defined refractory period. Single-units were classified as either narrow-spiking (putative interneurons) or broad-spiking (putative pyramidal cells) based on methods described in detail previously (Mitchell et al., 2007; Nandy et al., 2017). Specifically, only units with waveforms having a clearly defined peak *preceded* by a trough were potential candidates. The distribution of trough-to-peak duration was clearly bimodal (Hartigan's Dip Test, $p = 0.012$) (Hartigan and Hartigan, 1985). Units with trough-to-peak duration less than 225 μs were classified as narrow-spiking units; units with trough-to-peak duration greater than 225 μs were classified as broad-spiking units (Figure S1D; gray=narrow, black=broad).

Data was collected over 32 sessions (23 sessions in Monkey A, 9 in Monkey C), yielding a total of 413 single units (146 narrow-spiking, 267 broad-spiking) and 296 multi-unit clusters. Per session unit yield was considerably higher in Monkey C compared to

Monkey A, resulting in a roughly equal contribution of both monkeys toward the population data.

Task, Stimuli and Inclusion Criteria

Stimuli were presented on a computer monitor placed 57 cm from the eye. Eye position was continuously monitored with an infrared eye tracking system (ISCAN ETL-200). Trials were aborted if eye position deviated more than 1° (degree of visual angle, 'dva') from fixation. Experimental control was handled by NIMH Cortex software (http://www.cortex.salk.edu/). Eye-position (all sessions) and pupil diameter (18/32 sessions) data were concurrently recorded and stored using the MAP system.

Receptive Field Mapping: At the beginning of each recording session, neuronal RFs were mapped using subspace reverse correlation in which Gabor (eight orientations, 80% luminance contrast, spatial frequency 1.2 cycles/degree, Gaussian half-width 2°) or ring stimuli (80% luminance contrast) appeared at 60 Hz while the monkeys maintained fixation. Each stimulus appeared at a random location selected from an 11x11 grid with 1° spacing in the appropriate visual quadrant. Spatial receptive maps were obtained by applying reverse correlation to the evoked local field potential (LFP) signal at each recording site. For each spatial location in the 11x11 grid, we calculated the time-averaged power in the stimulus evoked LFP (0-200ms after each stimulus flash) at each recording site. The resulting spatial map of LFP power was taken as the spatial RF at the recording site. For the purpose of visualization, the spatial RF maps were smoothed using spline interpolation and displayed as stacked contours plots of the smoothed maps

(Figure S1G). All RFs were in the lower visual quadrant (lower-left in Monkey A, lower-right in Monkey C) and with eccentricities between 2 and 7 dva.

Current Source Density Mapping: In order to estimate the laminar identity of each recording channel, we used a current source-density (CSD) mapping procedure (Mitzdorf, 1985). Monkeys maintained fixation while 100% luminance contrast ring stimuli were flashed (30ms) centered at the estimated RF overlap region across all channels. The size of the ring was scaled to about three-quarters of the estimated diameter of the RF. CSD was calculated as the second spatial derivative of the flash-triggered LFPs (Figure S1E). The resulting time-varying traces of current across the cortical layers can be visualized as CSD maps (Figure S1F; maps have been spatially smoothed with a Gaussian kernel for aid in visualization). Red regions depict current sinks in the corresponding region of the cortical laminae; blue regions depict current sources. The input layer (Layer 4) was identified as the first current sink followed by a reversal to current source. The superficial (Layers 1-3) and deep (Layers 5-6) layers had opposite sink-source patterns. LFPs and spikes from the corresponding recording channels were then assigned to one of three layers: superficial, input or deep.

Attention task: In the main experiment, monkeys had to perform an attention-demanding orientation change-detection task (Figure 1A). While the monkey maintained fixation, two achromatic Gabor stimuli (orientation optimized per recording session, spatial frequency 1.2 cycles/degree, 6 contrasts randomly chosen from an uniform distribution of luminance contrasts, $c = [10, 18, 26, 34, 42, 50\%]$) were flashed on for 200 ms and off for a variable period chosen from a uniform distribution between 200-400 ms. One of the Gabors was flashed at the receptive field overlap region, the other at a location

of equal eccentricity across the vertical meridian. At the beginning of a block of trials, the monkey was spatially cued ('instruction trials') to covertly attend to one of these two spatial locations. During these instruction trials, the stimuli were only flashed at the spatially cued location. At an unpredictable time drawn from a truncated exponential distribution (minimum 1 s, maximum 5 s, mean 3 s), one of the two stimuli changed in orientation. The monkey was rewarded for making a saccade to the location of orientation change. The monkey was rewarded for only those saccades where the saccade onset time was within a window of 100-400 ms after the onset of the orientation change. The orientation change occurred at the cued location with 95% probability and at the uncued location with 5% probability ('foil trials'). We controlled task difficulty by varying the degree of orientation change (Δ_{ori}), which was randomly chosen from one of the following: 1, 2, 3, 4, 6, 8, 10 and 12°. The orientation change in the foil trials was fixed at 4°. These foil trials allowed us to assess the extent to which the monkey was using the spatial cue, with the expectation that there would be an impairment in performance and slower reaction times compared to the case in which the change occurred at the cued location. If no change occurred before 5s, the monkey was rewarded for maintaining fixation ('catch trials', 13% of trials). We refer to all stimuli at the baseline orientation as 'non-targets' and the stimulus flash with the orientation change as the 'target'.

Inclusion criteria: Of the 413 single units, we included only a subset of neurons that were visually responsive for further analysis. For each neuron we calculated its baseline firing-rate for each attention condition (attend into RF ['attend-in' or 'IN'], attend away from RF ['attend-away' or 'AWAY']) from a 200ms window before a stimulus flash. We also calculated the neuron's contrast response function for both attention conditions

(Figure S1H). This was calculated as the firing rate over a window between 60-200 ms after stimulus onset and averaged across all stimulus flashes (restricted to non-targets) of a particular contrast separately for each attention condition. A neuron was considered visually responsive if any part of the contrast response curves exceeded the baseline rate by 4 standard deviations for both attention conditions. This left us with 274 single units (84 narrow-spiking, 190 broad-spiking) and 217 multi-unit clusters for further analysis.

Data analysis

Behavioral Analysis: For each orientation change condition Δ_{ori}, we calculated the hit rate as the ratio of the number of trials in which the monkey correctly identified the target by making a saccadic eye-movement to the location of the target over the number of trials in which the target was presented. The hit rate as a function of Δ_{ori}, yields a behavioral psychometric function (Figure 1B). We performed this analysis independently for each recording day for each monkey, yielding a similar but distinct psychometric function for every session. Psychometric functions were fitted with a smooth logistic function (Prins and Kingdom, 2018). Error bars were obtained by a jackknife procedure (20 jackknives, 5% of trials left out for each jackknife). Performance for the foil trials were calculated similarly as the hit rate for trials in which the orientation change occurred at the un-cued location (Figure 1B, square symbol). For each fitted psychometric function in both the attend-in and attend-away conditions, we calculated the threshold of the fitted logistic function (i.e. the Δ_{ori} at which performance was mid-way between the lower and upper asymptotes). Because the threshold of the fitted function always lies somewhere on the axis of Δ_{ori}, but not exactly at an orientation change presented to the subject, we

445 then defined the threshold condition as the subset of trials in which the orientation change
446 of the target stimulus was closest to the threshold of the fitted function (Figure 1B). We
447 restricted further analysis to this threshold condition. For this threshold condition we
448 identified the trials in which the monkey correctly identified the target as 'hit' trials and
449 those in which the monkey failed to identify the target as 'miss' trials. Analysis of behavior,
450 pupil diameter, and microsaccades was conducted on both the attend-in and attend-away
451 conditions; all electrophysiological analysis was applied only to the attend-in condition.

452 *Pupil Diameter*: The raw pupil diameter measurements from the infrared eye-
453 tracking system could differ across days due to external factors such as display monitor
454 illumination. To control for this, we normalized the raw data by a Z-score procedure
455 separately for each session (using the mean and standard deviation of all measurements
456 during the session). We analyzed normalized pupil diameter traces for hit and miss trials
457 in the threshold condition, over a time window from 100 ms before to 100 ms after all
458 stimulus presentations, excluding the first stimulus presentation in a trial. The first
459 stimulus was excluded to avoid pupil diameter changes due to the pupillary near response
460 caused by acquiring fixation (McDougal and Gamlin, 2015). The pupil diameter was
461 averaged over this time period and compared across conditions using bootstrap
462 estimation and *t*-test. Distribution violin plots were generated using kernel density
463 estimation (Hoffmann, 2015) (bandwidth(hit) = 0.0801, bandwidth(miss) = 0.0648).

464 *Microsaccade Analysis:* Saccadic eye-movements were detected using ClusterFix
465 (König and Buffalo, 2014). We identified microsaccades by filtering for eye movements
466 with amplitudes between 0.1 and 1 degree of visual angle. We then split all trials in the
467 threshold condition into two groups: those in which a microsaccade was detected in the

400ms preceding the target stimulus presentation, and those without a detected microsaccade. We calculated the hit rate for trials within those two groups. For all trials in which a target stimulus was presented at the attended location, we determined the direction of all microsaccades in the 400ms period preceding target presentation, relative to both the attended and unattended stimuli. The relative microsaccade direction was defined as the angle between two vectors: the one defined by the eye positions at the beginning and end of the microsaccade, and the vector from the initial eye position to the center of the stimulus (calculated separately for attended and unattended stimuli). Relative microsaccade directions were grouped into 12 bins from 0-360°. The distribution of relative microsaccade directions were calculated separately for correct and incorrect trials, relative to both the attended and unattended stimuli (Figure S2A).

We next created a null distribution of relative microsaccade direction. This was done by pooling together microsaccades from correct and incorrect trials and then sampling with replacement from this pooled data (bootstrap procedure (Efrom and Tibshirani, 1993); 1000 samples). The number of microsaccades chosen for each sample was the same as the number in correct or incorrect trials respectively. These bootstrapped samples were used to create 99.5% confidence intervals for the count of microsaccades expected in each of the 12 bins. A bin was considered significantly different from chance if it's true count fell outside this confidence interval.

We calculated microsaccade rate for an entire trial by dividing the total number of detected microsaccades in the whole trial by the trial length (6995 total trials). The Pearson correlation between microsaccade rate and mean normalized pupil diameter (see above) for the trial was calculated for all trials with pupil diameter data, regardless

of trial type or outcome (Figure S2B). Not pictured in Figure S2B but included in correlation analysis were trials with a mean normalized pupil diameter greater than 2 or less than -2 (~4% of trials). Only 4 of these trials were longer than 1 s, out of which 2 trials contained detected microsaccades.

Firing Rate: Firing rates were normalized per neuron to that neuron's maximum stimulus-evoked response to each contrast before being combined across contrasts and trial types. We averaged stimulus-evoked firing rates from 60-260 ms following non-target or target stimulus presentations. We used bootstrapped estimation to compare firing rates in hit and miss trials in a paired comparison. This was done for all single and multi-unit clusters, as well as broad- and narrow-spiking single-units in each layer. Firing rates were also compared across hit and miss trials by paired *t*-test for each group. PSTH of firing rates were calculated in 30ms bins shifted in 5ms increments.

Fano factor: Trial-to-trial variability was estimated by the Fano-factor, which is the ratio of the variance of the spike counts across trials over the mean of the spike counts. The Fano factor was calculated over non-overlapping 20ms time bins in a window from 200ms prior to each non-target flash onset to 200ms after each non-target flash onset for hit and miss trials in the threshold condition. To compare across conditions, we calculated the Fano factor modulation index (MI), defined as

$$\mathrm{MI} = \frac{FF_{hit} - FF_{miss}}{FF_{hit} + FF_{miss}}$$

where FF_{hit} and FF_{miss} represent the Fano factor for a given unit in hit and miss trials respectively at each point in time with respect to non-target stimulus onset. For broad-spiking neurons in the superficial layer the Fano factor MI was averaged from 0-60ms

prior to non-target stimulus onset and compared across trial types in the threshold condition.

Pairwise Phase Consistency (PPC): We calculated PPC (Vinck et al., 2010) for single and multi-units in the non-target pre-stimulus period (0-200ms preceding onset) in trials in the threshold condition. Although PPC is unbiased by spike count, we set a threshold of 50 spikes for analysis so that only units with enough spikes for a reliable estimate of PPC were included (superficial: $n = 26$, input: $n = 41$, deep: $n = 64$). LFP phase was calculated using Morlet wavelets. PPC for each unit was calculated for the phase of the LFP recorded on the same channel and averaged in three frequency bands (3-12 Hz, 15-25 Hz, and 30-80 Hz). PPC was calculated separately for hit and miss trials and compared across trial outcomes by t-test, corrected for multiple comparisons.

Spike-spike coherence (SSC): For each recording session, all spikes recorded from visually responsive single and multi-units in each layer were combined into a single spike train for that layer (layer multi-unit). SSC was calculated for each of the three possible pairs of layer multi-units in each session for both the pre-stimulus (0-200 ms preceding stimulus onset) and stimulus evoked period (60-260 ms following stimulus onset) separately for hit and miss trials using Chronux (NW = 1; K = 1; http://chronux.org) (Mitra, 2007; Mitra and Pesaran, 1999). To control for differences in firing rates across hit and miss trials we used a rate matching procedure (Mitchell et al., 2009). For estimation statistics, interlaminar SSC values was calculated for each frequency and subsequently averaged across three frequency bands: 3-12 Hz, 5-15 Hz, and 30-80 Hz and compared across hit and miss trials for each pair of layers in each recording session. For null-hypothesis testing, we calculated the SSC modulation index, defined as

$$\mathrm{MI} = \frac{SSC_{hit} - SSC_{miss}}{SSC_{hit} + SSC_{miss}}$$

The SSC MI was calculated for each frequency and subsequently averaged across three frequency bands: 3-12 Hz, 5-15 Hz, and 30-80 Hz. MI values for each frequency band were compared to zero by t-test, Bonferroni corrected for multiple comparisons. We tested for interaction effects with a three-factor ANOVA, with frequency, pair of layers, and time window (pre or post stimulus) as factors. We calculated a shuffled distribution of SSC by shuffling the trial identities of the spikes in one of the layers in the pair. We then calculated SSC with the shuffled trial identities. This procedure was repeated 10 times to create the shuffled distribution.

GLM quantification: To compare how well our results can predict behavioral performance we fit a GLM to the response of the monkeys in trials in the threshold condition (Davis et al., 2020). We included five regressors in our analysis: (1) average pupil diameter during the trial, (2) number of microsaccades in the pre-target window (0-400ms before target stimulus onset), and average target-evoked multi-unit firing rate in the (3) superficial, (4) input, and (5) deep layers. We calculated the average target-evoked firing rate by averaging the firing rate of all single- and multi-units in a given layer 60-260ms after target stimulus onset in each trial. In order to be able to compare weights across regressors, each regressor was transformed into a z-score before being included in the model. We fit the GLM using a logit link function, using the predictors to regress the categorical binary trial outcome (hit or miss). A total of 309 trials were included in the GLM.

FIGURE LEGENDS

Figure 1. Orientation change detection task at perceptual threshold

(**A**) Schematic of task structure. The monkey initiated a trial by fixating on the center of the screen. Two Gabor stimuli (represented by oriented lines) were presented for 200 ms and then turned off for 200-400ms. This was repeated until, at an unpredictable time, one of the stimuli changed orientation. The monkey could report having seen the change by making an eye movement to the location of the target stimulus to receive a reward (hit trials). If the monkey failed to report the orientation change and maintained fixation on the center of the screen it was not rewarded (miss trials). Before a block of trials, the monkey was cued as to which stimulus was likely to undergo the change (95% valid cue). In 5% of trials the orientation change occurred at the other location (foil trials). (**B**) Example behavioral psychometric function from one recording session and attention condition. Behavioral performance (hit rate, circles) is presented as a function of orientation change. Data was fitted with a logistic function. The threshold condition, trials with performance halfway between the upper and lower asymptotes of the logistic function, is indicated by the orange box. Error bars represent standard deviation calculated with a jackknife procedure (20 jackknives). The square symbol indicates foil trial performance.

Figure 2. Hit trials have larger pupil diameter whereas microsaccades more often precede misses

(**A**) Normalized pupil diameter for hit and miss trails in the threshold condition. 0 ms corresponds to stimulus onset. Mean +/- s.e.m. (**B**) Distribution of pupil diameter values associated with hit and miss trials. Pupil diameter was averaged from 100ms before to 100ms after non-target stimulus onset. Violin plots were generated using kernel smoothing (See Experimental Procedures). Error bars represent 95% confidence intervals for the mean of each distribution, and the mean difference (blue, right axes). *Inset*: zoomed in view of the mean difference between hit and miss trials. Black bar represents a 95% confidence interval of the mean difference. Shaded region reflects the distribution of the bootstrapped estimation of the mean difference. (**C**) Histogram of mean pupil diameter around the time of stimulus onset (calculated as in **B**). Orange and gray lines represent the mean pupil diameter for hit and miss trials respectively. (**D**) Hit rate for trials with (*left*, 387 trials) and without (*right*, 1336 trials) a microsaccade detected in the time window 0-400ms before target onset. There is a significantly lower hit rate in trials with a microsaccade ($p < 0.0001$, X^2-test).

Figure 3. Target stimuli evoke higher firing rates in hit trials

Rows correspond to different layers (top=superficial, middle=input, bottom=deep). (**A**) Population (single and multi-unit) non-target PSTH of visually responsive neurons for the hit (orange) and miss (dark-gray) trials in the threshold condition (mean +/- s.e.m). (**B**) As in **A** but for target stimuli. (**C**) Bootstrapped estimation of the paired mean difference in target stimulus-evoked firing rate across hit and miss trials in the time window 60-260ms (red dotted box in **B**) after target stimulus onset. Shaded regions represent the bootstrapped estimation of the paired mean difference in firing rate (hit - miss), and black lines are 95% confidence intervals. Plots include data from both single and multi-units, separated by layer (top=superficial, middle=input, bottom=deep). (**D**) As in **C**, bootstrapped estimation of the paired mean difference in firing rate for hit trials compared to miss trials in the target stimulus-evoked period, but only for single-units broken up by cell class (gold=broad, teal=narrow).

Figure 4. Broad-spiking neurons in the superficial layer have decreased variability in hit trials

(**A**) Rows correspond to different layers (top=superficial, middle=input, bottom=deep). The Fano Factor of broad-spiking putative excitatory neurons for the hit and miss trials in the threshold condition (mean +/- s.e.m). There is a significant decrease in variability for the hit trials prior to stimulus onset only in the superficial layer. 0 ms corresponds to non-target stimulus onset. The average Fano Factor within a 60ms time-window (red dashed box) prior to stimulus onset is plotted in **B**. (**B**) *Top:* Fano Factor modulation index for each broad-spiking neurons recorded in each layer, averaged in the 60ms preceding stimulus onset. *Bottom:* Bootstrapped estimation of the mean difference of the Fano Factor modulation index from zero in each of the three layers. Colored curves represent the estimated bootstrapped distribution. Black dots and lines reflect the mean and 95% confidence intervals of the distributions.

Figure 5. Deep layer neurons are phase-locked to low-frequency rhythms in miss trials

(**A**) Pairwise phase consistency (PPC) of single and multi-units in each layer to the local field potential (LFP) signal recorded from the same channel in hit and miss trials at threshold. PPC was calculated in the pre-stimulus period (0-200 ms before stimulus onset). Dashed red line indicates a PPC of 0, below which there is no consistent relationship between spikes and LFP phase. (**B**) Bootstrapped estimation plot for the paired mean difference in PPC for deep layer neurons over three frequency bands: 3-12Hz, 15-25Hz, 30-80Hz. Curves represent the bootstrapped distribution for the paired difference, and black dots and vertical lines represent the mean and 95% confidence intervals for the paired mean difference

Figure 6. Greater interlaminar coherence in hit trials in the pre-stimulus period
Interlaminar spike-spike coherence in the pre-stimulus period (0-200ms prior to stimulus onset). Rows correspond to different pairs of layers (*top*=superficial-input, *middle*=superficial-deep, *bottom*=input-deep). (**A**) Multi-unit interlaminar spike-spike coherence (SSC) calculated in the 200ms before non-target stimulus onset in hit and miss trials (solid lines, mean +/- s.e.m). Firing rates were matched across hit and miss trials. Dashed lines represent coherence calculated with shuffled trial identities (mean +/- s.e.m). (**B**) Bootstrapped estimation plot for the paired mean difference in SSC for each pair of layers averaged over three frequency bands : 3-12Hz, 15-25Hz, 30-80Hz. Curves represent the bootstrapped distribution for the paired difference, and black dots and vertical lines represent the mean and 95% confidence intervals for the paired mean difference.

Figure 7. Greater interlaminar coherence in hit trials in the stimulus-evoked period
Interlaminar spike-spike coherence in the stimulus evoked period (60-260ms after stimulus onset). Same conventions as in Figure 6.

Figure 8. Summary of results
Hit trials have a larger pupil diameter in both the pre-stimulus and stimulus-evoked time periods. In the pre-stimulus period, hits are characterized by decreased variability in superficial layer broad-spiking neurons, less phase-locking of deep layer neurons to low-frequency LFPs, and greater interlaminar spike-spike coherence between the superficial and deep layers. Microsaccades in the pre-stimulus period are associated with a much lower hit rate. Stimuli evoke higher firing rates across all three layers in hits. The stimulus-evoked period is associated with greater interlaminar spike-spike coherence between the input layer and the superficial and deep layers.

Figure S1. Laminar recordings in V4
(**A**) An artificial dura (AD) chamber is shown over dorsal V4 in the right hemisphere of Monkey A. The native dura mater was resected and replaced with a silicone based artificial dura, thereby providing an optically clear window into the cortex. Scale bar = 5mm. (**B**) An enlarged view of the boxed region in **A** clearly shows the sulci and the microvasculature. sts = superior temporal sulcus, lu = lunate sulcus, io = inferior occipital sulcus. Area V4 lies on the pre-lunate gyrus between the superior temporal and lunate sulci. Scale bar = 2mm. (**C**) Electrophysiology setup: a plastic stabilizer with a circular aperture is secured in place inside the chamber such that the aperture is centered over the pre-lunate gryus. A 16-channel linear array electrode (electrode spacing 150 μm) is positioned over the center of the gyrus and lowered into the cortex under microscopic guidance. The microvasculature pattern was used as a reference to target different cortical sites across recording sessions. (**D**) Example recording session in monkey C depicting 12 single unit waveforms (mean +/- s.e.m.) isolated along the cortical column. Gray waveforms correspond to narrow-spiking putative interneurons and black waveforms correspond to broad-spiking putative excitatory units. (**E**) Stimulus triggered local field potentials (LFPs) obtained by flashing 30ms high contrast ring stimuli in the receptive field of a V4 cortical column. LFP traces averaged across all stimulus repeats are shown color-coded as being part of either the superficial (green), input (gray) or deep (pink) layers. Layer assignment was done after current source-density analysis. (**F**) Current source-density (CSD) calculated as the second spatial derivative of the stimulus triggered LFPs and displayed as a colored map. The x-axis represents time from stimulus onset; the y-axis represents cortical depth oriented such that the pial surface is at the top and the white matter is at the bottom. Red hues represent current sink, blue hues represent current source. The input layer is identified as the first current sink followed by a reversal to current source. The superficial and deep layers have the opposite sink-source pattern. The CSD map has been spatially smoothed for visualization. (**G**) Stacked contour plots show spatial receptive fields (RFs) mapped along each contact point in the laminar probe. The spatial receptive fields were obtained by applying reverse

correlation to the LFP power evoked by sparse pseudo-random sequences of Gabor stimuli. The RFs are well aligned, indicating perpendicular penetration down a cortical column. Zero depth represents the center of the input layer as estimated from the CSD. (**H**) Contrast response functions – spikes rate as a function of stimulus contrast – are shown for 2 example units identified in a single recording session in Monkey A. Red and blue traces correspond to the attend-in to RF and attend-away from RF conditions respectively. The dotted lines represent the corresponding background firing-rates. The dashed lines are 4 standard deviations above baseline. A unit was considered as visually responsive, if the contrast response functions exceeded this threshold in both the attention conditions. Mean +/- s.e.m. Panels are reproduced from Nandy et al. (2017).

Figure S2. Microsaccades are preferentially directed towards the target in correct trials and have a slight correlation with pupil diameter

Data is presented for all trials, regardless of orientation change (not just the threshold condition). (**A**) The histograms represent the direction of microsaccades relative to the attended stimulus (left column) or unattended stimulus (right column) in correct (top row) and incorrect (bottom row) trials. Black lines represent the mean (solid) and 99.5% confidence interval (dashed) of the bootstrapped null distribution estimated by pooling correct and incorrect microsaccades. $* \mathrm{p} < 0.005$. *Inset:* Schematic for calculation of relative microsaccade direction. Microsaccade is represented by the gray arrow (**B**) Scatterplot of microsaccade rate versus mean normalized pupil diameter, shows a small but statistically significant relationship between the two quantities ($r^2 = 0.006$, $p < 0.001$). Each dot is color-coded by trial length. 4% of trials with mean pupil diameter >2 or <-2 not shown.

Figure S3. Firing rates for individual neurons

Target stimulus-evoked normalized firing rates in hit and miss trials for each recorded single and multi-unit cluster in hit and miss trials. Clusters are divided by layer: left=superficial, middle=input, right=deep. Related to Figure 3B. Each line represents the mean firing rate in response to target stimuli in hit and miss trials for a given unit. Data is color coded by unit type (gold=broad, teal=narrow, gray=multi-unit). See Experimental Procedures for normalization method.

Figure S4. Additional PPC data

(**A-B**) *Top:* Raw PPC values calculated for clusters recorded in the superficial (**A**) and (**B**) input layers in hit and miss trials, averaged into three frequency bands, 3-12 Hz, 15-25 Hz, and 30-80 Hz. PPC was calculated using the LFP recorded on the same channel as the spikes. *Bottom:* Bootstrapped estimation of the paired mean difference in PPC across hit and miss trials for each frequency band. Note that although there appears to be a difference in high-frequency PPC in the superficial layer, this population does not have significantly positive PPC in either condition, indicating that there is no phase-locking in either hits or misses. (**C**) Raw PPC values for neurons recorded in the deep layer in hit and miss trials, averaged into the same 3 frequency bands. Related to Figure 5B.

Table 1: Corresponding Null-Hypothesis Testing Results

Figure	Null-Hypothesis Test	P-Value
2B (pupil diameter)	*t*-test (unpaired)	$p = 6.63624\text{e}-09$
2C (microsaccades)	X^2-test	$p \ll 0.0001$
3B (target-evoked firing rate, single and multi-units)	*t*-test (paired) Bonferoni Corrected for 3 comparisons, $\alpha = 0.0166$	Superficial: $p = 4.19108\text{e}-05$ Input: $p = 1.10838\text{e}-11$ Deep: $p = 1.75826\text{e}-11$
3C (target-evoked firing rate, broad-spiking)	*t*-test (paired) Bonferoni Corrected for 3 comparisons, $\alpha = 0.0166$	Superficial: $p = 0.0526902$ Input: $p = 0.000124947$ Deep: $p = 0.00119012$
3C (target-evoked firing rate, narrow-spiking)	*t*-test (paired) Bonferoni Corrected for 3 comparisons, $\alpha = 0.0166$	Superficial: $p = 0.103689$ Input: $p = 0.00570757$ Deep: $p = 0.00393437$
4B (Fano Factor modulation index)	*t*-test (unpaired) Bonferoni Corrected for 3 comparisons, $\alpha = 0.0166$	Superficial: $p = 0.0102155$ Input: $p > 0.05$ Deep: $p > 0.05$
5B (deep PPC)	*t*-test (paired) Bonferoni Corrected for 3 comparisons, $\alpha = 0.0166$	3-12 Hz: $p = 0.0142$ 15-25 Hz: $p = 0.4064$ 30-80 Hz: $p = 0.3600$
6B (top, superficial-input SSC modulation index)	*t*-test Bonferoni Corrected for 3 comparisons, $\alpha = 0.0166$	3-12 Hz: $p = 0.925338$ 15-25 Hz: $p = 0.107304$ 30-80 Hz: $p = 0.00394525$
6B (middle, superficial-deep SSC modulation index)	*t*-test Bonferoni Corrected for 3 comparisons, $\alpha = 0.0166$	3-12 Hz: $p = 0.0125919$ 15-25 Hz: $p = 0.00116552$ 30-80 Hz: $p = 0.00142568$
6B (bottom, input-deep SSC modulation index)	*t*-test Bonferoni Corrected for 3 comparisons, $\alpha = 0.0166$	3-12 Hz: $p = 0.260698$ 15-25 Hz: $p = 0.0358178$ 30-80 Hz: $p = 0.0325516$
7B (top, superficial-input SSC modulation index)	*t*-test Bonferoni Corrected for 3 comparisons, $\alpha = 0.0166$	3-12 Hz: $p = 0.00344279$ 15-25 Hz: $p = 3.17111\text{e}-05$ 30-80 Hz: $p = 0.00396824$
7B (middle, superficial-deep SSC modulation index)	*t*-test Bonferoni Corrected for 3 comparisons, $\alpha = 0.0166$	3-12 Hz: $p = 0.0164846$ 15-25 Hz: $p = 0.0890114$ 30-80 Hz: $p = 0.00441928$
7B (bottom, input-deep SSC modulation index)	*t*-test Bonferoni Corrected for 3 comparisons, $\alpha = 0.0166$	3-12 Hz: $p = 0.241036$ 15-25 Hz: $p = 0.00140176$ 30-80 Hz: $p = 6.84271\text{e}-05$
S43B (superficial PPC)	*t*-test (paired) Bonferoni Corrected for 3 comparisons, $\alpha = 0.0166$	3-12 Hz: $p = 0.8307$ 15-25 Hz: $p = 0.2812$ 30-80 Hz: $p = 0.0037$*
S43C (input PPC)	*t*-test (paired) Bonferoni Corrected for 3 comparisons, $\alpha = 0.0166$	3-12 Hz: $p = 0.3440$ 15-25 Hz: $p = 0.2517$ 30-80 Hz: $p = 0.1881$

* Although this p-value is significant, the PPC in both conditions is below 0, indicating there is no phase-locking in either condition (Vinck et al., 2010).

Table 2: GLM Values

Variable (Z-Scored)	Estimated Coefficient	P-Value
Pupil Diameter	0.11754	$p = 0.32869$
Pretarget Microsaccades	-1.3116	$p = 6.0757e - 08$
Target Superficial FR	0.22414	$p = 0.091946$
Target Input FR	0.3276	$p = 0.020068$
Target Deep FR	0.11399	$p = 0.45762$

AUTHOR CONTRIBUTIONS

MPJ and ASN conceptualized the project. ASN collected the data and supervised the project. MPM analyzed the data, with assistance from SD and IB. MPM, SD, ASN, MPJ, and JHR wrote the manuscript.

ACKNOWLEDGEMENTS

This research was supported by NIH R01 EY021827 to JHR and ASN, NARSAD Young Investigator Grant, Ziegler Foundation Grant, Yale Orthwein Scholar Funds & Lawrence Family Young Investigator Funds to ASN, NIH R00 EY025026 to MPJ, and by NEI core grants for vision research P30 EY019005 to the Salk Institute and P30 EY026878 to Yale University. MM was supported by training grants T32-NS007224 and T32-NS041228 to Yale University. We would like to thank Catherine Williams and Mat LeBlanc for excellent animal care.

REFERENCES

Abbas, A.I., Sundiang, M.J.M., Henoch, B., Morton, M.P., Bolkan, S.S., Park, A.J., Harris, A.Z., Kellendonk, C., and Gordon, J.A. (2018). Somatostatin Interneurons Facilitate Hippocampal-Prefrontal Synchrony and Prefrontal Spatial Encoding. Neuron 100, 926-939.e923.

Aston-Jones, G., and Cohen, J.D. (2005). An integrative theory of locus coeruleus-norepinephrine function: adaptive gain and optimal performance. Annu Rev Neurosci 28, 403-450.

Beatty, J., and Lucero-Wagoner, B. (2000). The pupillary system. Handbook of psychophysiology 2.

Beeler, G.W. (1967). Visual threshold changes resulting from spontaneous saccadic eye movements. Vision Research 7, 769-775.

Calin-Jageman, R.J., and Cumming, G. (2019). Estimation for Better Inference in Neuroscience. eneuro 6, ENEURO.0205-0219.2019.

Cohen, M.R., and Maunsell, J.H. (2009). Attention improves performance primarily by reducing interneuronal correlations. Nat Neurosci 12, 1594-1600.

Connors, B.W., and Gutnick, M.J. (1990). Intrinsic firing patterns of diverse neocortical neurons. Trends Neurosci 13, 99-104.

Davis, Z.W., Muller, L., Martinez-Trujillo, J., Sejnowski, T., and Reynolds, J.H. (2020). Spontaneous travelling cortical waves gate perception in behaving primates. Nature 587, 432-436.

Dehaene, S., and Changeux, J.-P. (2011). Experimental and Theoretical Approaches to Conscious Processing. Neuron 70, 200-227.

Desimone, R., and Duncan, J. (1995). Neural mechanisms of selective visual attention. Annu Rev Neurosci 18, 193-222.

Dicke, P.W., Chakraborty, S., and Thier, P. (2008). Neuronal correlates of perceptual stability during eye movements. European Journal of Neuroscience 27, 991-1002.

Douglas, R.J., and Martin, K.A.C. (2004). NEURONAL CIRCUITS OF THE NEOCORTEX. Annual Review of Neuroscience 27, 419-451.

Douglas, R.J., and Martin, K.A.C. (2007). Mapping the Matrix: The Ways of Neocortex. Neuron 56, 226-238.

Efrom, B., and Tibshirani, R.J. (1993). An introduction to the bootstrap. Champman and Hall/CRC.

Fries, P. (2009). Neuronal Gamma-Band Synchronization as a Fundamental Process in Cortical Computation. Annual Review of Neuroscience 32, 209-224.

Fries, P., Reynolds, J.H., Rorie, A.E., and Desimone, R. (2001). Modulation of Oscillatory Neuronal Synchronization by Selective Visual Attention. Science 291, 1560.

Fries, P., Womelsdorf, T., Oostenveld, R., and Desimone, R. (2008). The effects of visual stimulation and selective visual attention on rhythmic neuronal synchronization in macaque area V4. The Journal of neuroscience : the official journal of the Society for Neuroscience 28, 4823-4835.

773 Goodale, M.A., and Milner, A.D. (1992). Separate visual pathways for perception and
774 action. Trends in Neurosciences 15, 20-25.
775 Hafed, Z.M., and Krauzlis, R.J. (2010). Microsaccadic suppression of visual bursts in
776 the primate superior colliculus. The Journal of neuroscience : the official journal
777 of the Society for Neuroscience 30, 9542-9547.
778 Harris, K.D., and Thiele, A. (2011). Cortical state and attention. Nature Reviews
779 Neuroscience 12, 509-523.
780 Hartigan, J.A., and Hartigan, P.M. (1985). The dip test of unimodality. The annals of
781 Statistics, 70-84.
782 Herman, W.X., Smith, R.E., Kronemer, S.I., Watsky, R.E., Chen, W.C., Gober, L.M.,
783 Touloumes, G.J., Khosla, M., Raja, A., Horien, C.L.*, et al.* (2017). A Switch and
784 Wave of Neuronal Activity in the Cerebral Cortex During the First Second of
785 Conscious Perception. Cerebral Cortex 29, 461-474.
786 Hess, E.H., and Polt, J.M. (1964). Pupil size in relation to mental activity during simple
787 problem-solving. Science 143, 1190-1192.
788 Hirsch, J.A., and Martinez, L.M. (2006). Laminar processing in the visual cortical column.
789 Curr Opin Neurobiol 16, 377-384.
790 Ho, J., Tumkaya, T., Aryal, S., Choi, H., and Claridge-Chang, A. (2019). Moving beyond
791 P values: data analysis with estimation graphics. Nature Methods 16, 565-566.
792 Hoffmann, H. (2015). violin.m - Simple violin plot using matlab default kernel density
793 estimation. (INRES (University of Bonn), Katzenburgweg 5, 53115 Germany.,).
794 Kawaguchi, Y. (1993). Groupings of nonpyramidal and pyramidal cells with specific
795 physiological and morphological characteristics in rat frontal cortex. Journal of
796 Neurophysiology 69, 416-431.
797 König, S.D., and Buffalo, E.A. (2014). A nonparametric method for detecting fixations
798 and saccades using cluster analysis: removing the need for arbitrary thresholds.
799 Journal of neuroscience methods 227, 121-131.
800 Levitt, H. (1971). Transformed Up-Down Methods in Psychoacoustics. The Journal of
801 the Acoustical Society of America 49, 467-477.
802 Livingstone, M.S., and Hubel, D.H. (1981). Effects of sleep and arousal on the
803 processing of visual information in the cat. Nature 291, 554-561.
804 Lowet, E., Gomes, B., Srinivasan, K., Zhou, H., Schafer, R.J., and Desimone, R. (2018).
805 Enhanced Neural Processing by Covert Attention only during Microsaccades
806 Directed toward the Attended Stimulus. Neuron 99, 207-214.e203.
807 Markram, H., Toledo-Rodriguez, M., Wang, Y., Gupta, A., Silberberg, G., and Wu, C.
808 (2004). Interneurons of the neocortical inhibitory system. Nature reviews
809 Neuroscience 5, 793-807.
810 Marshel, J.H., Kim, Y.S., Machado, T.A., Quirin, S., Benson, B., Kadmon, J., Raja, C.,
811 Chibukhchyan, A., Ramakrishnan, C., Inoue, M.*, et al.* (2019). Cortical layer–
812 specific critical dynamics triggering perception. Science 365, eaaw5202.
813 McAdams, C.J., and Maunsell, J.H. (1999). Effects of attention on orientation-tuning
814 functions of single neurons in macaque cortical area V4. The Journal of
815 neuroscience : the official journal of the Society for Neuroscience 19, 431-441.
816 McCormick, D.A., and Bal, T. (1997). SLEEP AND AROUSAL: Thalamocortical
817 Mechanisms. Annual Review of Neuroscience 20, 185-215.

818 McCormick, D.A., Connors, B.W., Lighthall, J.W., and Prince, D.A. (1985). Comparative
819 electrophysiology of pyramidal and sparsely spiny stellate neurons of the
820 neocortex. J Neurophysiol 54, 782-806.
821 McCormick, D.A., Nestvogel, D.B., and He, B.J. (2020). Neuromodulation of Brain State
822 and Behavior. Annual Review of Neuroscience 43, null.
823 McDougal, D.H., and Gamlin, P.D. (2015). Autonomic control of the eye. Compr Physiol
824 5, 439-473.
825 McGinley, M.J., David, S.V., and McCormick, D.A. (2015). Cortical Membrane Potential
826 Signature of Optimal States for Sensory Signal Detection. Neuron 87, 179-192.
827 Migliore, M., and Shepherd, G.M. (2005). An integrated approach to classifying neuronal
828 phenotypes. Nature Reviews Neuroscience 6, 810-818.
829 Mitchell, J.F., Sundberg, K.A., and Reynolds, J.H. (2007). Differential attention-
830 dependent response modulation across cell classes in macaque visual area V4.
831 Neuron 55, 131-141.
832 Mitchell, J.F., Sundberg, K.A., and Reynolds, J.H. (2009). Spatial attention decorrelates
833 intrinsic activity fluctuations in macaque area V4. Neuron 63, 879-888.
834 Mitra, P. (2007). Observed brain dynamics (Oxford University Press).
835 Mitra, P.P., and Pesaran, B. (1999). Analysis of dynamic brain imaging data. Biophys J
836 76, 691-708.
837 Mitzdorf, U. (1985). Current source-density method and application in cat cerebral
838 cortex: investigation of evoked potentials and EEG phenomena. Physiol Rev 65,
839 37-100.
840 Moore, T., and Fallah, M. (2001). Control of eye movements and spatial attention. Proc
841 Natl Acad Sci U S A 98, 1273-1276.
842 Moore, T., and Zirnsak, M. (2017). Neural Mechanisms of Selective Visual Attention.
843 Annual Review of Psychology 68, 47-72.
844 Moran, J., and Desimone, R. (1985). Selective attention gates visual processing in the
845 extrastriate cortex. Science 229, 782-784.
846 Moreno-Bote, R., Beck, J., Kanitscheider, I., Pitkow, X., Latham, P., and Pouget, A.
847 (2014). Information-limiting correlations. Nat Neurosci 17, 1410-1417.
848 Mountcastle, V.B. (1997). The columnar organization of the neocortex. Brain 120 (Pt
849 4), 701-722.
850 Nandy, A.S., Nassi, J.J., and Reynolds, J.H. (2017). Laminar Organization of Attentional
851 Modulation in Macaque Visual Area V4. Neuron 93, 235-246.
852 Nassi, J.J., Avery, M.C., Cetin, A.H., Roe, A.W., and Reynolds, J.H. (2015). Optogenetic
853 Activation of Normalization in Alert Macaque Visual Cortex. Neuron 86, 1504-
854 1517.
855 Nowak, L.G., Azouz, R., Sanchez-Vives, M.V., Gray, C.M., and McCormick, D.A. (2003).
856 Electrophysiological classes of cat primary visual cortical neurons in vivo as
857 revealed by quantitative analyses. J Neurophysiol 89, 1541-1566.
858 Pettine, W.W., Steinmetz, N.A., and Moore, T. (2019). Laminar segregation of sensory
859 coding and behavioral readout in macaque V4. Proceedings of the National
860 Academy of Sciences 116, 14749-14754.
861 Pins, D., and ffytche, D. (2003). The Neural Correlates of Conscious Vision. Cerebral
862 Cortex 13, 461-474.

Prins, N., and Kingdom, F.A.A. (2018). Applying the Model-Comparison Approach to Test Specific Research Hypotheses in Psychophysical Research Using the Palamedes Toolbox. Frontiers in Psychology 9.

Reimer, J., Froudarakis, E., Cadwell, Cathryn R., Yatsenko, D., Denfield, George H., and Tolias, Andreas S. (2014). Pupil Fluctuations Track Fast Switching of Cortical States during Quiet Wakefulness. Neuron 84, 355-362.

Ress, D., and Heeger, D.J. (2003). Neuronal correlates of perception in early visual cortex. Nat Neurosci 6, 414-420.

Reynolds, J.H., Pasternak, T., and Desimone, R. (2000). Attention increases sensitivity of V4 neurons. Neuron 26, 703-714.

Roe, Anna W., Chelazzi, L., Connor, Charles E., Conway, Bevil R., Fujita, I., Gallant, Jack L., Lu, H., and Vanduffel, W. (2012). Toward a Unified Theory of Visual Area V4. Neuron 74, 12-29.

Rohenkohl, G., Bosman, C.A., and Fries, P. (2018). Gamma Synchronization between V1 and V4 Improves Behavioral Performance. Neuron 100, 953-963.e953.

Ruiz, O., Lustig, B.R., Nassi, J.J., Cetin, A., Reynolds, J.H., Albright, T.D., Callaway, E.M., Stoner, G.R., and Roe, A.W. (2013). Optogenetics through windows on the brain in the nonhuman primate. J Neurophysiol 110, 1455-1467.

Schafer, R.J., and Moore, T. (2011). Selective attention from voluntary control of neurons in prefrontal cortex. Science 332, 1568-1571.

Schurger, A., Pereira, F., Treisman, A., and Cohen, J.D. (2010). Reproducibility distinguishes conscious from nonconscious neural representations. Science 327, 97-99.

Siapas, A.G., Lubenov, E.V., and Wilson, M.A. (2005). Prefrontal Phase Locking to Hippocampal Theta Oscillations. Neuron 46, 141-151.

Spitzer, H., Desimone, R., and Moran, J. (1988). Increased attention enhances both behavioral and neuronal performance. Science 240, 338-340.

Steriade, M., Nuñez, A., and Amzica, F. (1993). A novel slow (< 1 Hz) oscillation of neocortical neurons in vivo: depolarizing and hyperpolarizing components. The Journal of neuroscience : the official journal of the Society for Neuroscience 13, 3252-3265.

Tang, L., and Higley, M.J. (2020). Layer 5 Circuits in V1 Differentially Control Visuomotor Behavior. Neuron 105, 346-354.e345.

van Vugt, B., Dagnino, B., Vartak, D., Safaai, H., Panzeri, S., Dehaene, S., and Roelfsema, P.R. (2018). The threshold for conscious report: Signal loss and response bias in visual and frontal cortex. Science 360, 537.

Vinck, M., van Wingerden, M., Womelsdorf, T., Fries, P., and Pennartz, C.M. (2010). The pairwise phase consistency: a bias-free measure of rhythmic neuronal synchronization. NeuroImage 51, 112-122.

von Krosigk, M., Bal, T., and McCormick, D. (1993). Cellular mechanisms of a synchronized oscillation in the thalamus. Science 261, 361-364.

Watson, A.B. (1979). Probability summation over time. Vision Research 19, 515-522.

Wichmann, F.A., and Hill, N.J. (2001). The psychometric function: I. Fitting, sampling, and goodness of fit. Perception & Psychophysics 63, 1293-1313.

Wonders, C.P., and Anderson, S.A. (2006). The origin and specification of cortical interneurons. Nature reviews Neuroscience 7, 687-696.

909 Worden, M.S., Foxe, J.J., Wang, N., and Simpson, G.V. (2000). Anticipatory biasing of
910 visuospatial attention indexed by retinotopically specific alpha-band
911 electroencephalography increases over occipital cortex. The Journal of
912 neuroscience : the official journal of the Society for Neuroscience 20, Rc63.
913 Yerkes, R.M., and Dodson, J.D. (1908). The relation of strength of stimulus to rapidity
914 of habit-formation. Journal of Comparative Neurology and Psychology 18, 459-
915 482.
916 Zeng, H., and Sanes, J.R. (2017). Neuronal cell-type classification: challenges,
917 opportunities and the path forward. Nature Reviews Neuroscience 18, 530-546.
918 Zohary, E., Shadlen, M.N., and Newsome, W.T. (1994). Correlated neuronal discharge
919 rate and its implications for psychophysical performance. Nature 370, 140-143.
920 Zuber, B.L., and Stark, L. (1966). Saccadic suppression: elevation of visual threshold
921 associated with saccadic eye movements. Exp Neurol 16, 65-79.

922

Figure 1

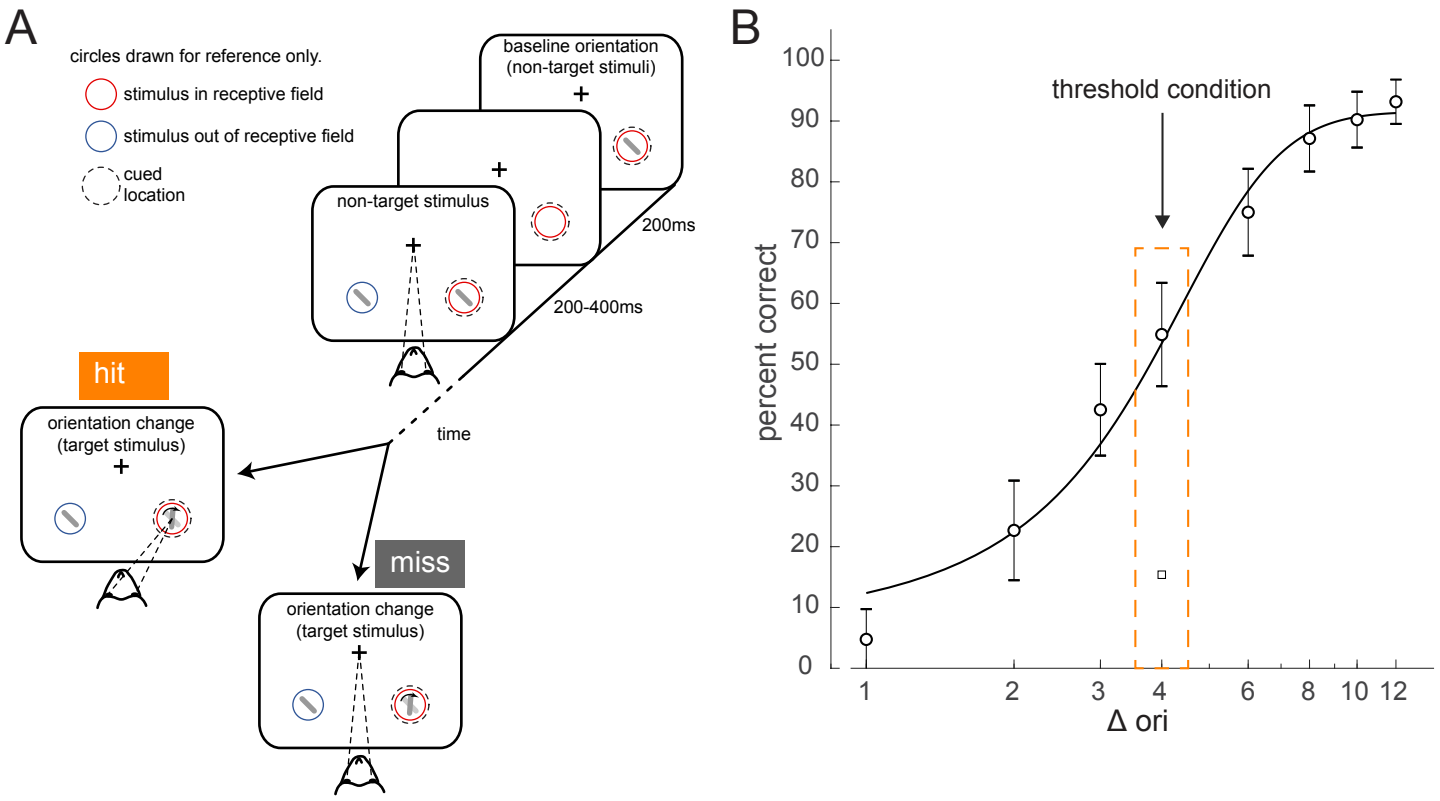

Figure 1. Orientation change detection task at perceptual threshold

(**A**) Schematic of task structure. The monkey initiated a trial by fixating on the center of the screen. Two Gabor stimuli (represented by oriented lines) were presented for 200 ms and then turned off for 200-400ms. This was repeated until, at an unpredictable time, one of the stimuli changed orientation. The monkey could report having seen the change by making an eye movement to the location of the target stimulus to receive a reward (hit trials). If the monkey failed to report the orientation change and maintained fixation on the center of the screen it was not rewarded (miss trials). Before a block of trials, the monkey was cued as to which stimulus was likely to undergo the change (95% valid cue). In 5% of trials the orientation change occurred at the other location (foil trials). (**B**) Example behavioral psychometric function from one recording session and attention condition. Behavioral performance (hit rate, circles) is presented as a function of orientation change. Data was fitted with a logistic function. The threshold condition, trials with performance halfway between the upper and lower asymptotes of the logistic function, is indicated by the orange box. Error bars represent standard deviation calculated with a jackknife procedure (20 jackknives). The square symbol indicates foil trial performance.

Figure 2

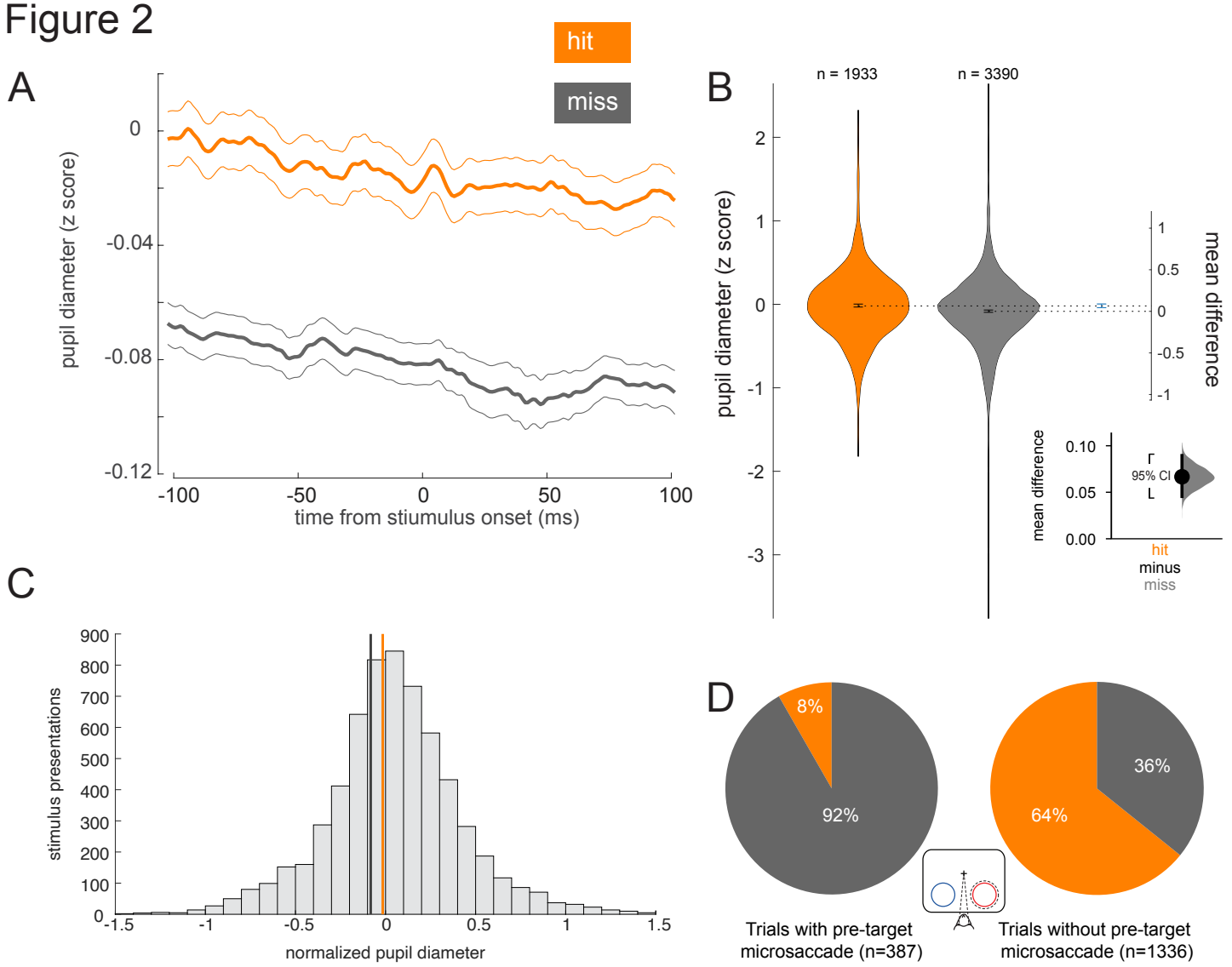

Figure 2. Hit trials have larger pupil diameter whereas microsaccades more often precede misses
(**A**) Normalized pupil diameter for hit and miss trails in the threshold condition. 0 ms corresponds to stimulus onset. Mean +/- s.e.m. (**B**) Distribution of pupil diameter values associated with hit and miss trials. Pupil diameter was averaged from 100ms before to 100ms after non-target stimulus onset. Violin plots were generated using kernel smoothing (See Experimental Procedures). Error bars represent 95% confidence intervals for the mean of each distribution, and the mean difference (blue, right axes). *Inset*: zoomed in view of the mean difference between hit and miss trials. Black bar represents a 95% confidence interval of the mean difference. Shaded region reflects the distribution of the bootstrapped estimation of the mean difference. (**C**) Histogram of mean pupil diameter around the time of stimulus onset (calculated as in **B**). Orange and gray lines represent the mean pupil diameter for hit and miss trials respectively. (**D**) Hit rate for trials with (*left*, 387 trials) and without (*right*, 1336 trials) a microsaccade detected in the time window 0-400ms before target onset. There is a significantly lower hit rate in trials with a microsaccade ($p<0.0001$, X^2-test).

Figure 3

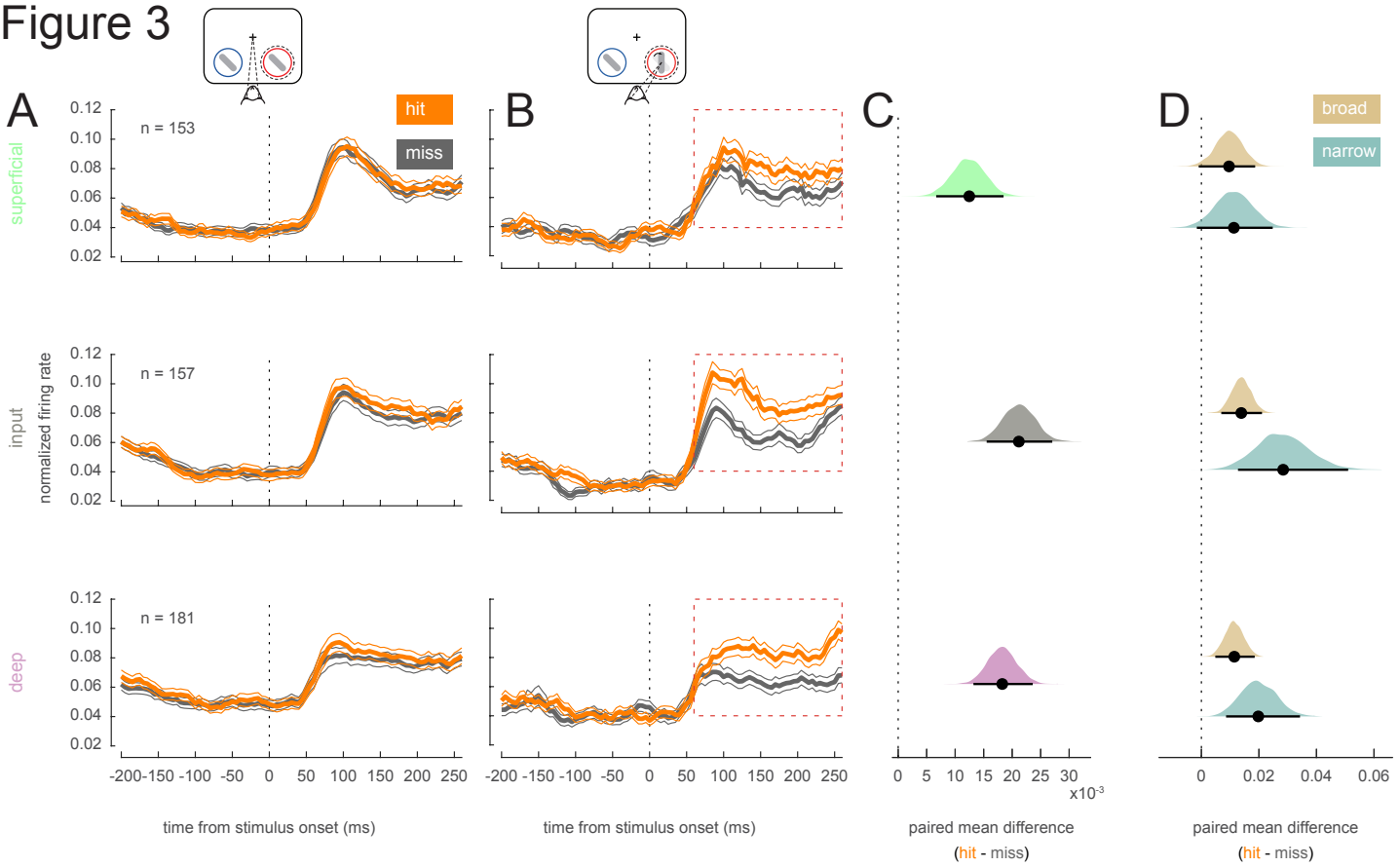

Figure 3. Target stimuli evoke higher firing rates in hit trials

Rows correspond to different layers (top=superficial, middle=input, bottom=deep). (**A**) Population (single and multi-unit) non-target PSTH of visually responsive neurons for the hit (orange) and miss (dark-gray) trials in the threshold condition (mean +/- s.e.m). (**B**) As in **A** but for target stimuli. (**C**) Bootstrapped estimation of the paired mean difference in target stimulus-evoked firing rate across hit and miss trials in the time window 60-260ms (red dotted box in **B**) after target stimulus onset. Shaded regions represent the bootstrapped estimation of the paired mean difference in firing rate (hit - miss), and black lines are 95% confidence intervals. Plots include data from both single and multi-units, separated by layer (top=superficial, middle=input, bottom=deep). (**D**) As in **C**, bootstrapped estimation of the paired mean difference in firing rate for hit trials compared to miss trials in the target stimulus-evoked period, but only for single-units broken up by cell class (gold=broad, teal=narrow).

Figure 4

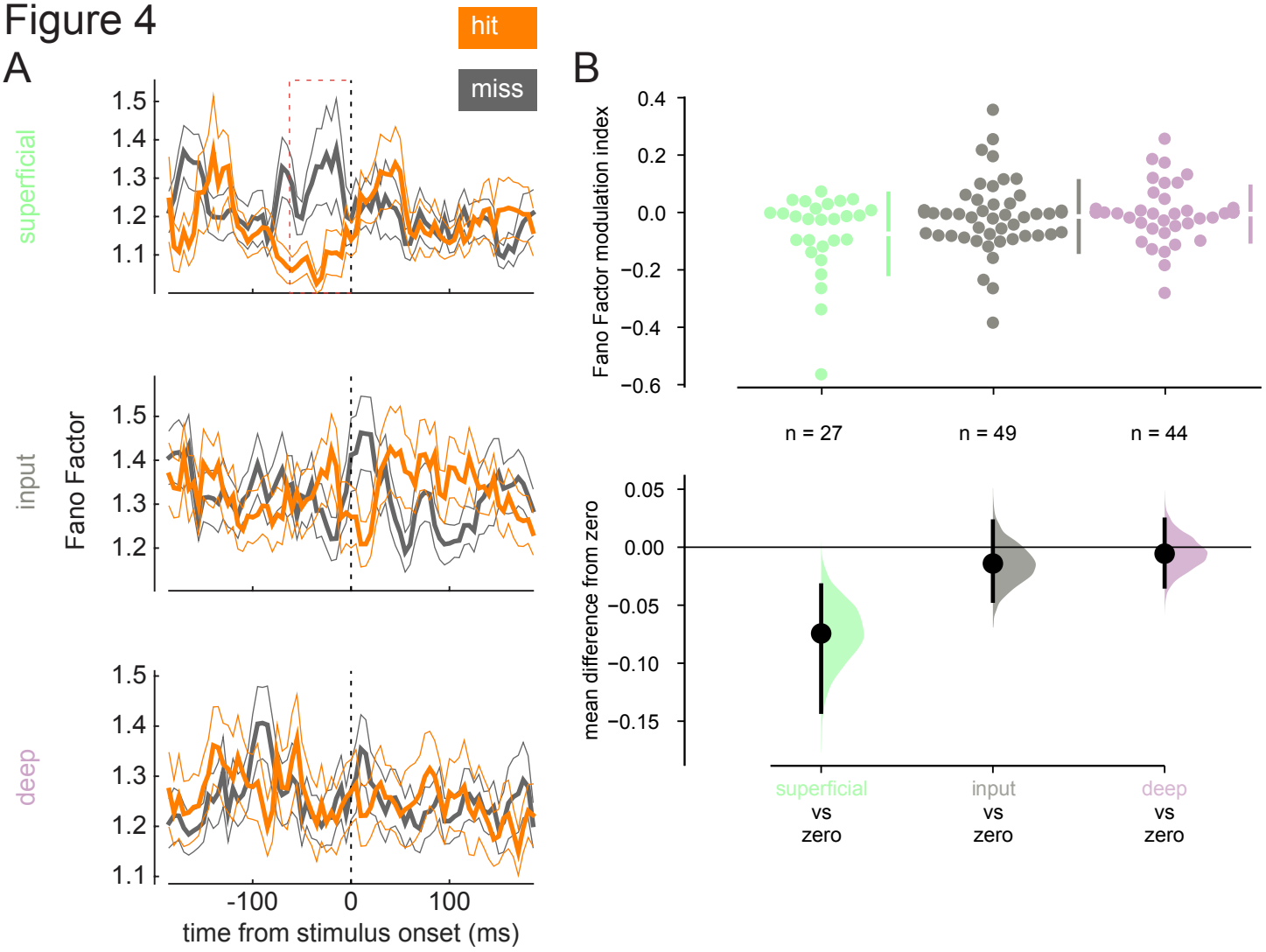

Figure 4. Broad-spiking neurons in the superficial layer have decreased variability in hit trials
(**A**) Rows correspond to different layers (top=superficial, middle=input, bottom=deep). The Fano Factor of broad-spiking putative excitatory neurons for the hit and miss trials in the threshold condition (mean +/- s.e.m). There is a significant decrease in variability for the hit trials prior to stimulus onset only in the superficial layer. 0 ms corresponds to non-target stimulus onset. The average Fano Factor within a 60ms time-window (red dashed box) prior to stimulus onset is plotted in **B**. (**B**) *Top:* Fano Factor modulation index for each broad-spiking neurons recorded in each layer, averaged in the 60ms preceding stimulus onset. *Bottom:* Bootstrapped estimation of the mean difference of the Fano Factor modulation index from zero in each of the three layers. Colored curves represent the estimated bootstrapped distribution. Black dots and lines reflect the mean and 95% confidence intervals of the distributions.

Figure 5

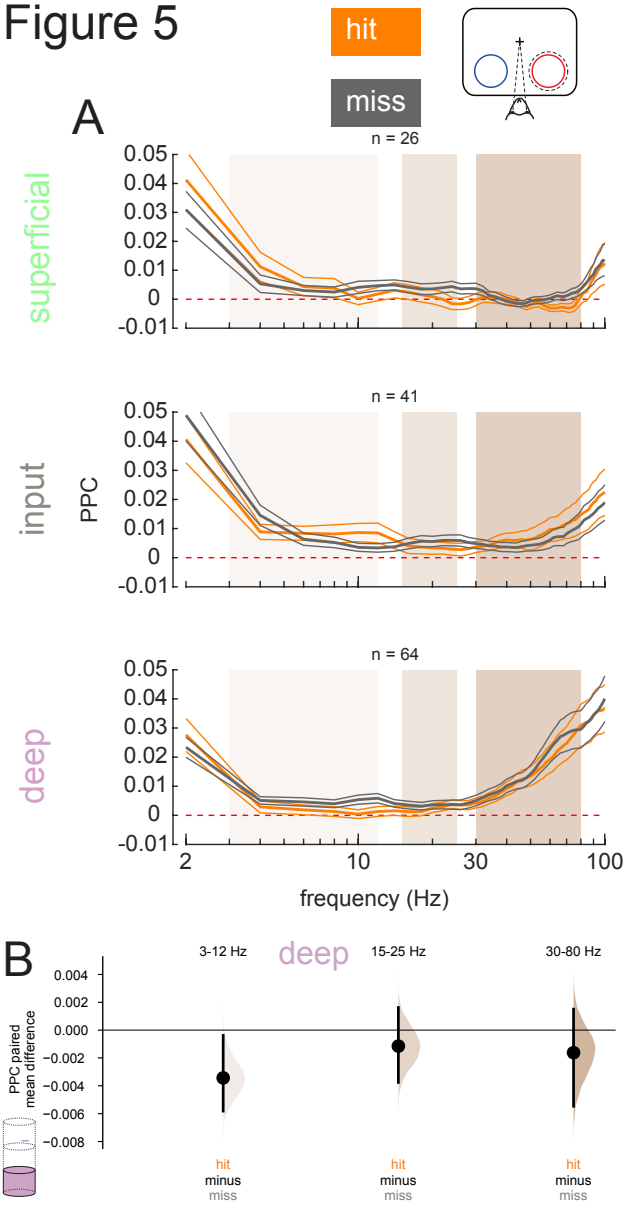

Figure 5. Deep layer neurons are phase-locked to low-frequency rhythms in miss trials
(**A**) Pairwise phase consistency (PPC) of single and multi-units in each layer to the local field potential (LFP) signal recorded from the same channel in hit and miss trials at threshold. PPC was calculated in the pre-stimulus period (0-200 ms before stimulus onset). Dashed red line indicates a PPC of 0, below which there is no consistent relationship between spikes and LFP phase. (**B**) Bootstrapped estimation plot for the paired mean difference in PPC for deep layer neurons over three frequency bands: 3-12Hz, 15-25Hz, 30-80Hz. Curves represent the bootstrapped distribution for the paired difference, and black dots and vertical lines represent the mean and 95% confidence intervals for the paired mean difference

Figure 6

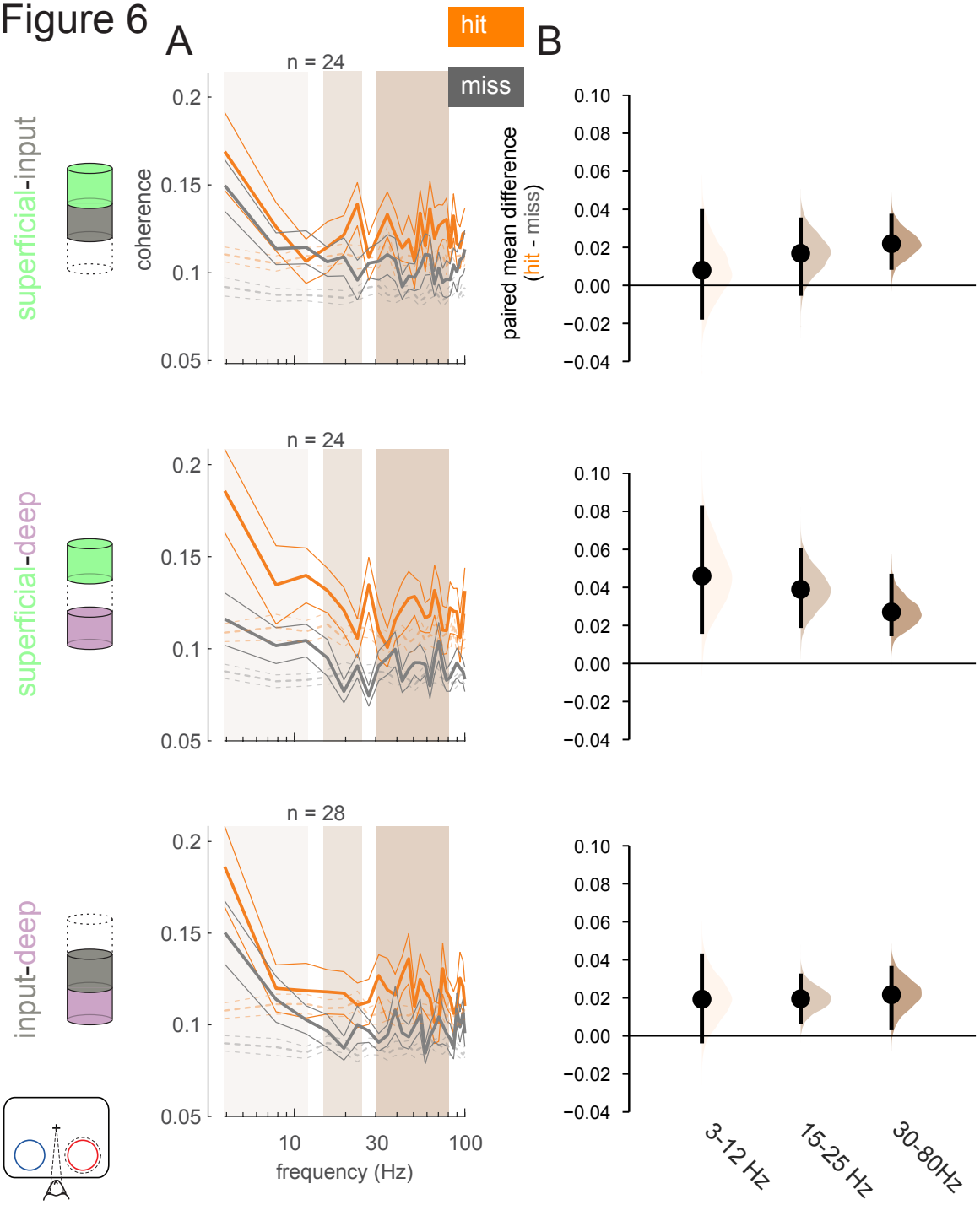

Figure 6. Greater interlaminar coherence in hit trials in the pre-stimulus period
Interlaminar spike-spike coherence in the pre-stimulus period (0-200ms prior to stimulus onset). Rows correspond to different pairs of layers (*top*=superficial-input, *middle*=superficial-deep, *bottom*=input-deep). (**A**) Multi-unit interlaminar spike-spike coherence (SSC) calculated in the 200ms before non-target stimulus onset in hit and miss trials (solid lines, mean +/- s.e.m). Firing rates were matched across hit and miss trials. Dashed lines represent coherence calculated with shuffled trial identities (mean +/- s.e.m). (**B**) Bootstrapped estimation plot for the paired mean difference in SSC for each pair of layers averaged over three frequency bands : 3-12Hz, 15-25Hz, 30-80Hz. Curves represent the bootstrapped distribution for the paired difference, and black dots and vertical lines represent the mean and 95% confidence intervals for the paired mean difference.

Figure 7

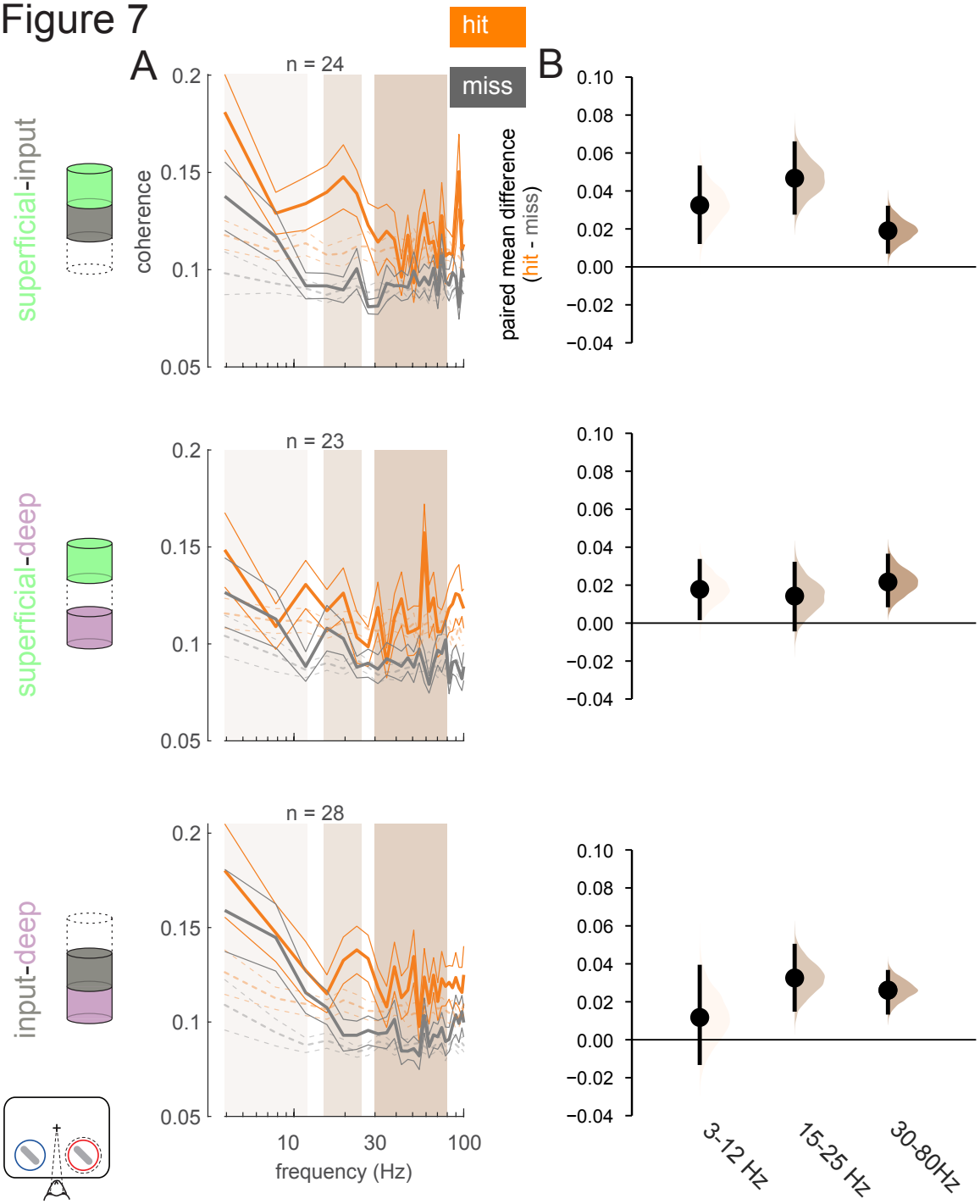

Figure 7. Greater interlaminar coherence in hit trials in the stimulus-evoked period
Interlaminar spike-spike coherence in the stimulus evoked period (60-260ms after stimulus onset). Same conventions as in Figure 6.

Figure 8

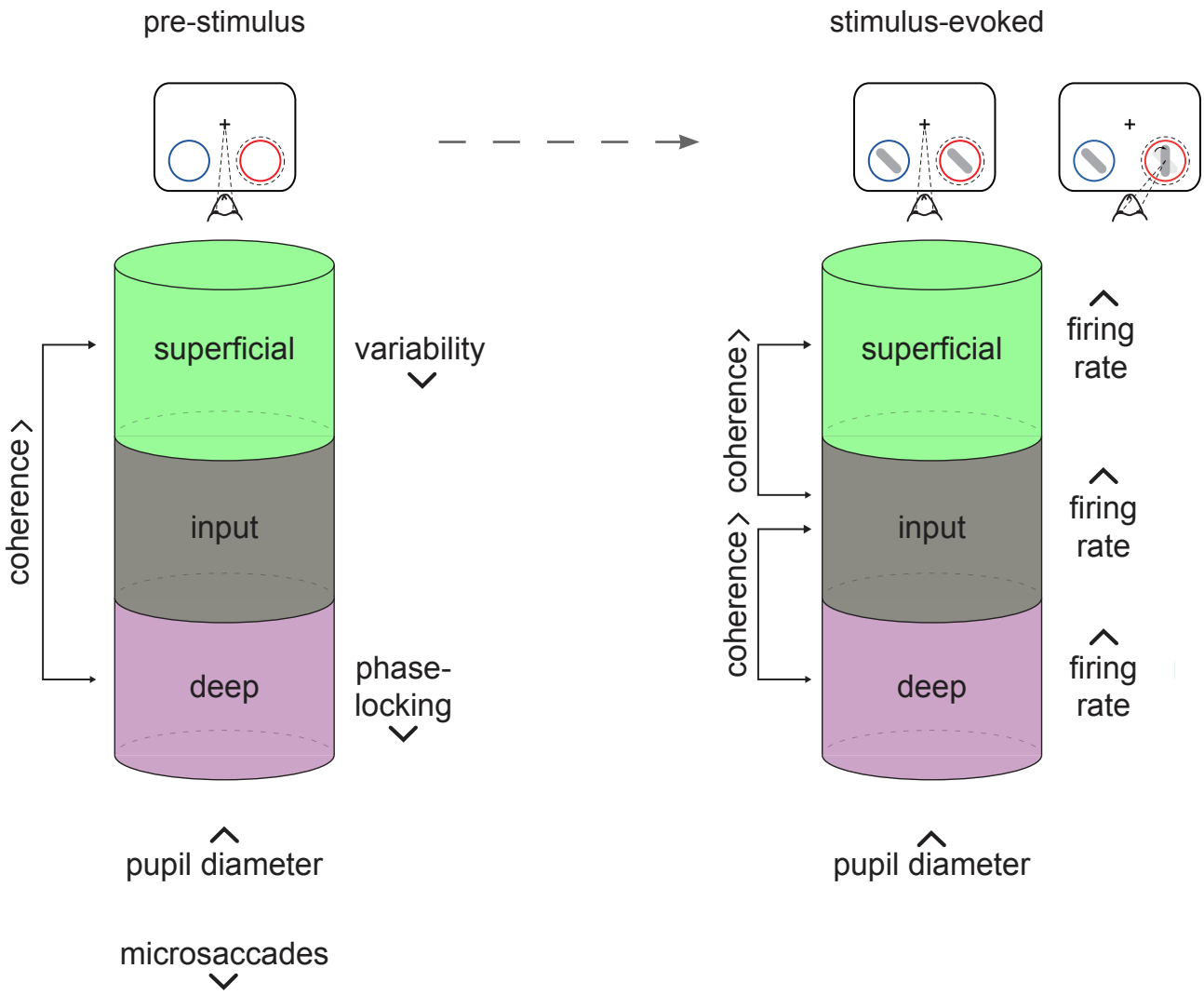

Figure 8. Summary of results
Hit trials have a larger pupil diameter in both the pre-stimulus and stimulus-evoked time periods. In the pre-stimulus period, hits are characterized by decreased variability in superficial layer broad-spiking neurons, less phase-locking of deep layer neurons to low-frequency LFPs, and greater interlaminar spike-spike coherence between the superficial and deep layers. Microsaccades in the pre-stimulus period are associated with a much lower hit rate. Stimuli evoke higher firing rates across all three layers in hits. The stimulus-evoked period is associated with greater interlaminar spike-spike coherence between the input layer and the superficial and deep layers.

Figure S1

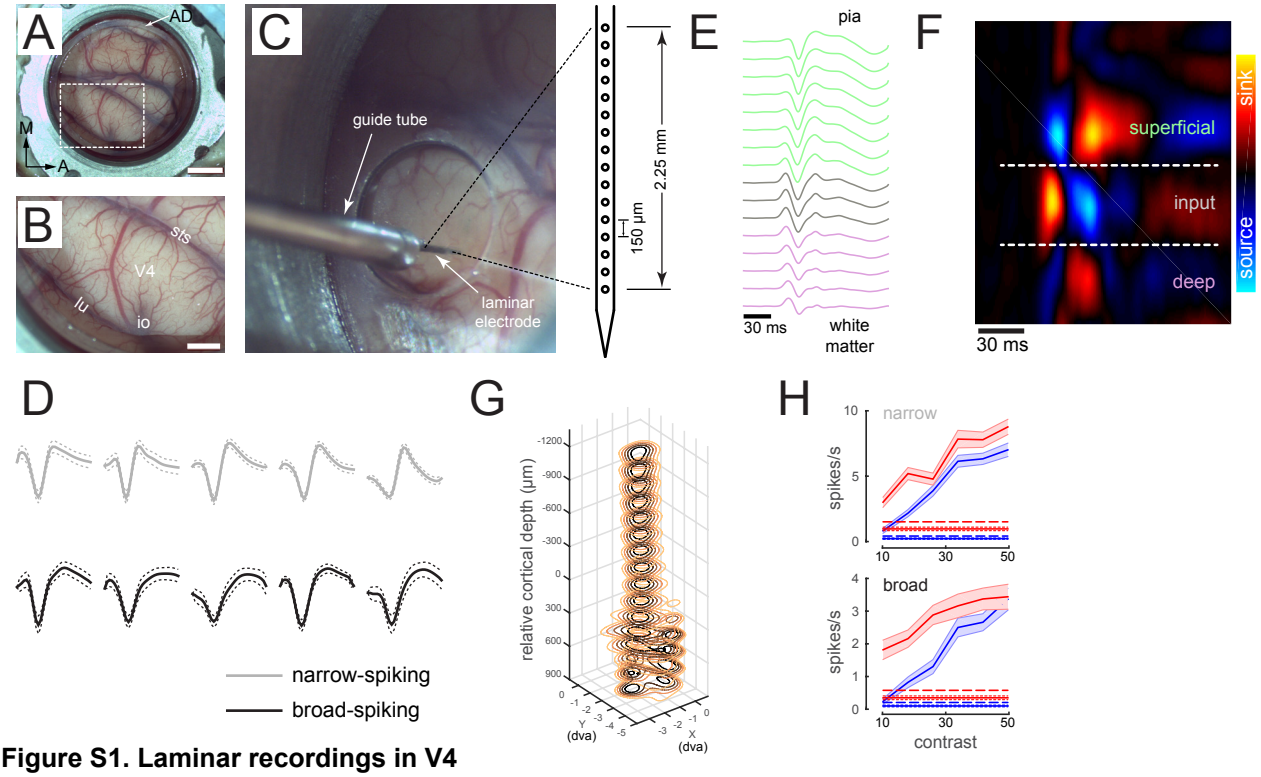

Figure S1. Laminar recordings in V4

(**A**) An artificial dura (AD) chamber is shown over dorsal V4 in the right hemisphere of Monkey A. The native dura mater was resected and replaced with a silicone based artificial dura, thereby providing an optically clear window into the cortex. Scale bar = 5mm. (**B**) An enlarged view of the boxed region in **A** clearly shows the sulci and the microvasculature. sts = superior temporal sulcus, lu = lunate sulcus, io = inferior occipital sulcus. Area V4 lies on the pre-lunate gyrus between the superior temporal and lunate sulci. Scale bar = 2mm. (**C**) Electrophysiology setup: a plastic stabilizer with a circular aperture is secured in place inside the chamber such that the aperture is centered over the pre-lunate gryus. A 16-channel linear array electrode (electrode spacing 150m) is positioned over the center of the gyrus and lowered into the cortex under microscopic guidance. The microvasculature pattern was used as a reference to target different cortical sites across recording sessions. (**D**) Example recording session in monkey C depicting 12 single unit waveforms (mean +/- s.e.m.) isolated along the cortical column. Gray waveforms correspond to narrow-spiking putative interneurons and black waveforms correspond to broad-spiking putative excitatory units. (**E**) Stimulus triggered local field potentials (LFPs) obtained by flashing 30ms high contrast ring stimuli in the receptive field of a V4 cortical column. LFP traces averaged across all stimulus repeats are shown color-coded as being part of either the superficial (green), input (gray) or deep (pink) layers. Layer assignment was done after current source-density analysis. (**F**) Current source-density (CSD) calculated as the second spatial derivative of the stimulus triggered LFPs and displayed as a colored map. The x-axis represents time from stimulus onset; the y-axis represents cortical depth oriented such that the pial surface is at the top and the white matter is at the bottom. Red hues represent current sink, blue hues represent current source. The input layer is identified as the first current sink followed by a reversal to current source. The superficial and deep layers have the opposite sink-source pattern. The CSD map has been spatially smoothed for visualization. (**G**) Stacked contour plots show spatial receptive fields (RFs) mapped along each contact point in the laminar probe. The spatial receptive fields were obtained by applying reverse correlation to the LFP power evoked by sparse pseudo-random sequences of Gabor stimuli. The RFs are well aligned, indicating perpendicular penetration down a cortical column. Zero depth represents the center of the input layer as estimated from the CSD. (**H**) Contrast response functions – spikes rate as a function of stimulus contrast – are shown for 2 example units identified in a single recording session in Monkey A. Red and blue traces correspond to the attend-in to RF and attend-away from RF conditions respectively. The dotted lines represent the corresponding background firing-rates. The dashed lines are 4 standard deviations above baseline. A unit was considered as visually responsive, if the contrast response functions exceeded this threshold in both the attention conditions. Mean +/- s.e.m. Panels are reproduced from Nandy et al. (2017).

Figure S2

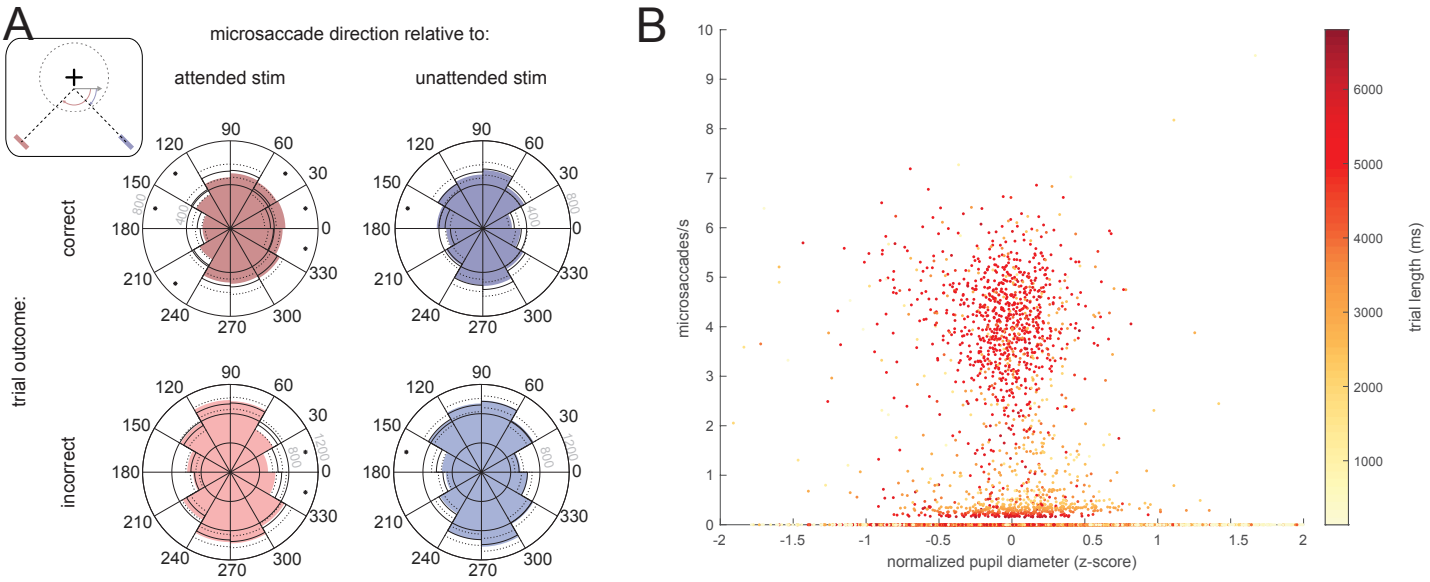

Figure S2. Microsaccades are preferentially directed towards the target in correct trials and have a slight correlation with pupil diameter

Data is presented for all trials, regardless of orientation change (not just the threshold condition). (**A**) The histograms represent the direction of microsaccades relative to the attended stimulus (left column) or unattended stimulus (right column) in correct (top row) and incorrect (bottom row) trials. Black lines represent the mean (solid) and 99.5% confidence interval (dashed) of the bootstrapped null distribution estimated by pooling correct and incorrect microsaccades. . *Inset:* Schematic for calculation of relative microsaccade direction. Microsaccade is represented by the gray arrow (**B**) Scatterplot of microsaccade rate versus mean normalized pupil diameter, shows a small but statistically significant relationship between the two quantities (r^2 = 0.006,). Each dot is color-coded by trial length. 4% of trials with mean pupil diameter >2 or <-2 not shown.

Figure S3

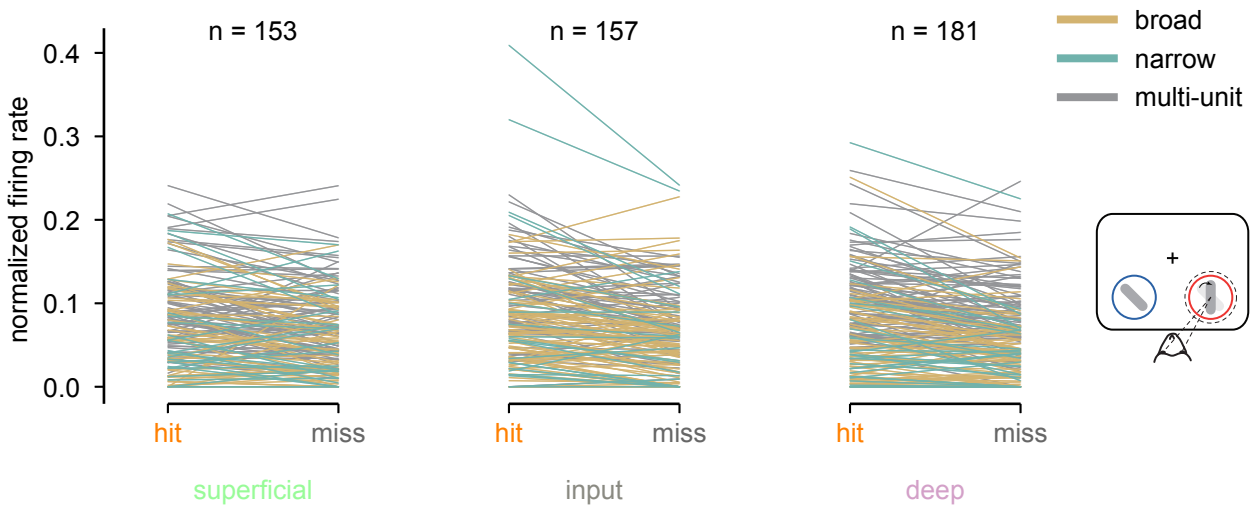

Figure S3. Firing rates for individual neurons

Target stimulus-evoked normalized firing rates in hit and miss trials for each recorded single and multi-unit cluster in hit and miss trials. Clusters are divided by layer: left=superficial, middle=input, right=deep. Related to Figure 3B. Each line represents the mean firing rate in response to target stimuli in hit and miss trials for a given unit. Data is color coded by unit type (gold=broad, teal=narrow, gray=multi-unit). See Experimental Procedures for normalization method.

Figure S4

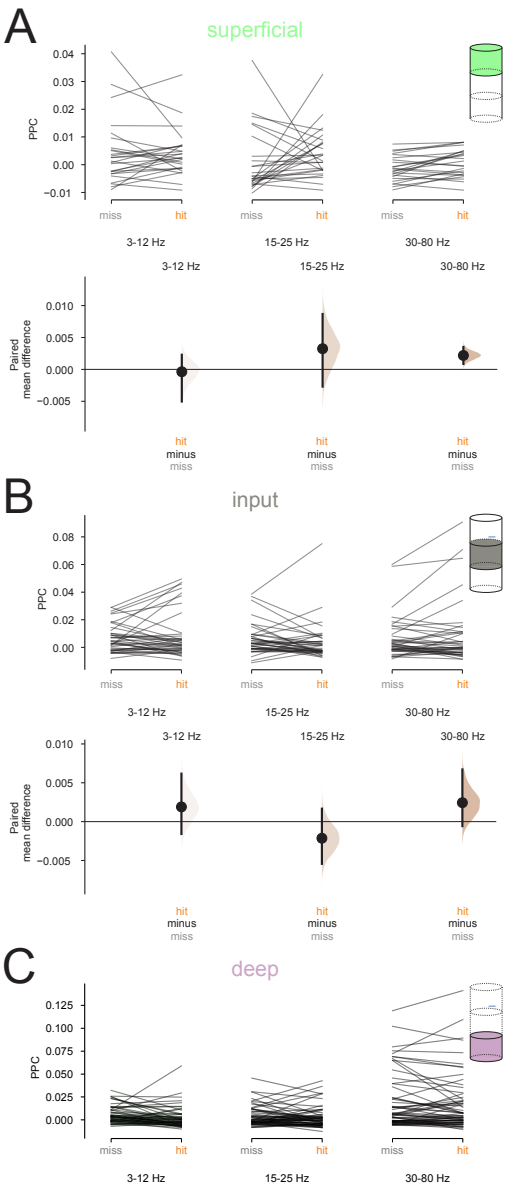

Figure S4. Additional PPC data

(**A-B**) *Top:* Raw PPC values calculated for clusters recorded in the superficial (**A**) and (**B**) input layers in hit and miss trials, averaged into three frequency bands, 3-12 Hz, 15-25 Hz, and 30-80 Hz. PPC was calculated using the LFP recorded on the same channel as the spikes. *Bottom:* Bootstrapped estimation of the paired mean difference in PPC across hit and miss trials for each frequency band. Note that although there appears to be a difference in high-frequency PPC in the superficial layer, this population does not have significantly positive PPC in either condition, indicating that there is no phase-locking in either hits or misses. (**C**) Raw PPC values for neurons recorded in the deep layer in hit and miss trials, averaged into the same 3 frequency bands. Related to Figure 5B.